Received: 9 March 2022 | Revised: 4 July 2022 | Accepted: 16 July 2022

DOI: 10.1002/adc2.113

ORIGINAL ARTICLE

WILEY

Controller parameterization and bias current reduction of active magnetic bearings for a flexible and gyroscopic spindle

Daniel Franz | **Jens Jungblut** | **Stephan Rinderknecht**

Institute for Mechatronic Systems, Technical University of Darmstadt, Darmstadt, Germany

Correspondence
Daniel Franz, Institute for Mechatronic Systems, Technical University of Darmstadt, Darmstadt, Germany.
Email: franz@ims.tu-darmstadt.de

Funding information
Bundesministerium für Wirtschaft und Energie, Grant/Award Numbers: 03ET6064A, 03EI3000A

Abstract

A magnetically levitated spindle was designed for fatigue testing of cylinders made of fiber reinforced plastic. In these fatigue tests, the speed of the cylinders is varied cyclically between 15,000 and 30,000 rpm until their mechanical failure occurs. Several eigenfrequencies have to be passed to reach the operational speed range. During long-term operation, the rotor of the spindle is prone to overheating due to various losses. One way of reducing the rotor temperature is to decrease the bias current of the radial active magnetic bearings. Since the bias current influences the dynamic behavior of the system, the control of the bearings has to be adapted as well. This article describes a controller design for the system with different bias currents to determine the smallest usable bias current. A detailed model of the plant is developed, which is then used to optimize the parameters of the utilized controller with a predefined structure using the weighted $\mathcal{H}_\infty$ norm as the objective function. Since the rotor is highly gyroscopic, its eigenfrequencies change with the rotational speed. To ensure that the system meets certain robustness criteria at all rotational speeds, the parameters of the controller are simultaneously optimized for the plant model at different speeds. This approach leads to a controller which can be used in the entire speed range without the need for gain scheduling. The functionality of the controller and the influence of the bias current on the rotor temperature are investigated through measurements.

KEYWORDS

active magnetic bearings, loss reduction, predefined controller structure, rotor dynamics

1 | INTRODUCTION

Outer-rotor flywheels, in which energy is stored as kinetic energy of the rotor, provide a possibility for short-term energy storage and load smoothing services. In this flywheel design, the rotor is a hubless hollow cylinder made of fiber reinforced plastic (FRP). All rotating components are integrated into the inner circumference of the FRP rotor. Two realized systems are described in References 1,2. The energy density of these systems increases with the radii of the rotor and

This is an open access article under the terms of the Creative Commons Attribution-NonCommercial License, which permits use, distribution and reproduction in any medium, provided the original work is properly cited and is not used for commercial purposes.
© 2022 The Authors. *Advanced Control for Applications: Engineering and Industrial Systems* published by John Wiley & Sons Ltd.

its rotational speed. Both lead to increased mechanical stress in the FRP.[3] Consequently, high stress in the material accompanies a high energy density of the energy storage. Charging and discharging of a flywheel leads to cyclic varying multiaxial mechanical stresses in the rotor, which can damage it over time.[3] To investigate the cycle stability and hence the lifetime of the FRP rotor of the flywheels, a test rig was designed and built to perform fatigue tests on thick-walled FRP cylinders, which serve as proxy specimens for the rotors. A cross section of the test rig is shown in Figure 1 on the left. The test rig is described in more detail in References 4,5. An outside view of the system is shown in Figure A1 in Appendix A. During a fatigue test, the rotational speed of the FRP cylinder is periodically varied from 15,000 to 30,000 rpm until it fails or a maximum cycle count of 200,000 is reached. In the latter case, the test takes approximately 3 months. A segmented steel ring is placed inside the FRP cylinder to create mechanical stress comparable to the one in the rotor of an outer-rotor flywheel. The FRP cylinder with the steal segments is called specimen in the following. For overload tests, the rotational speed can be ramped up to 40,000 rpm, but this article will focus on the normal operation up to 30,000 rpm.

The outer diameter of the FRP cylinder is 190 mm. Hence, at 30,000 rpm the surface speed is about 298 m/s. To reduce drag and subsequent heating of the specimen, all tests take place in a vacuum. The vacuum chamber also serves as a containment. As a further security measure, a steel tube is placed inside the containment as a liner to absorb the kinetic energy of fragments from a failed specimen.[6,7] A driving spindle is placed on top of the containment. In the spindle, which is also evacuated, a 30 kW permanent magnet synchronous machine (PMSM) is used to accelerate and decelerate the rotor. The specimen is connected to the driving spindle via an aluminum hub and a shaft coupling. A predetermined breaking point in form of a taper was incorporated into the hub to protect the spindle in case of a specimen failure. This flexible taper has a major impact on the rotor dynamics, which will be discussed further in Section 2. To avoid excessive wear, the rotor is supported by active magnetic bearings (AMBs), which also allow for active control of the rotor dynamics.

One of the two radial AMBs is placed above and the other below the PMSM. Both are heteropolar AMBs with eight poles and a differential winding scheme (DWS) (cf. Reference 8). The axial AMB is located above the upper radial AMB. The position sensors which are needed for the control of the AMBs are positioned at both ends of the rotor of the driving spindle. Further position sensors are located inside the specimen. These sensors are used to monitor the position and radial enlargement of the specimen during operation. The test rig is placed on spring elements to reduce and dampen the solid body eigenfrequencies of the stator.

The test rig is heating up due to various energy losses during operation. In the stator, these are composed of ohmic and remagnetization losses in the PMSM and the AMBs. The losses on the rotor are dominated by remagnetization losses. Losses due to air friction can be neglected because of the operation in vacuum.[4] The stator is cooled using a water-cooling system. However, the loss energy on the rotor is only ineffectively transferred to the stator via radiation. This can lead to

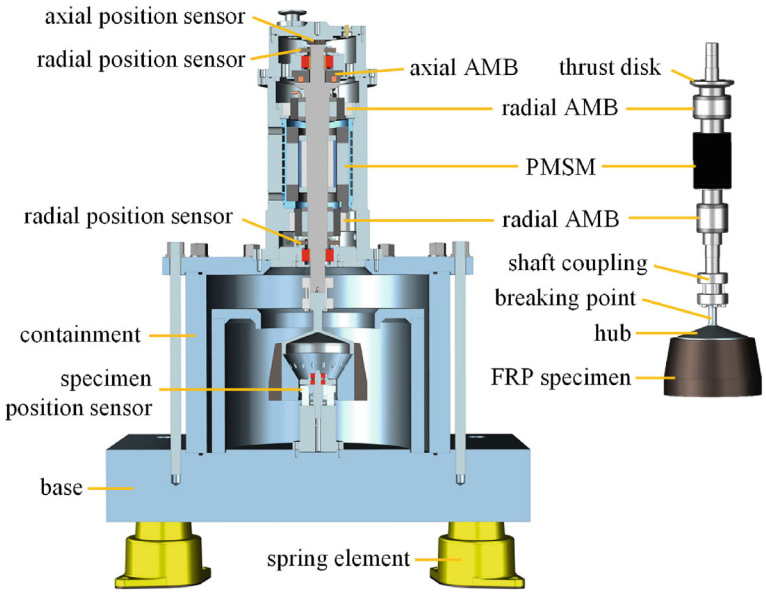

FIGURE 1 Left: Cross section of the test rig; right: Rotor with the specimen

overheating of the rotor during long-term operation and can damage the magnets of the PMSM and the specimen. Hence, losses on the rotor have to be minimized. A significant portion of the remagnetization losses on the rotor are the rotational losses in the heteropolar radial AMBs.[4,5] These are largely determined by the bias current I_B, which is used to linearize the characteristic of the AMBs (cf. Reference 8) and to increase their force slew-rate at low control currents (cf. Reference 9). In the discussed system, I_B can be adjusted by the amplifier of the AMBs allowing for a reduction of the steady state rotor temperature to a certain extent without changing the hardware of the system. However, if a very low I_B is chosen or it is set to zero and the control current I_c is allowed to be bigger than I_B, a nonlinear controller has to be used. Nonlinear controller designs based on feedback linearization,[10–12] sliding mode control,[12] backstepping,[9,13] and control Lyapunov functions,[9] among others, can be used for an AMB with low or zero bias current. Normally, I_B is set to a fixed value but I_B and the controller can also be adjusted depending on I_c [14] or the rotor deflection.[15,16] However, using nonlinear control increases the difficulty in determining the stability and robustness of the controlled system. Furthermore, to utilize these control schemes $I_c > I_B$ has to be possible, which is not the case for AMB with a DWS as used in the test rig. Hence, this article focuses on linear control, where the control current of the AMB must always be smaller than the fixed bias current.

The goal of this article is therefore to determine the smallest I_B for the radial AMBs still allowing for a robust operation using a linear controller. To achieve this, the control of the AMBs has to be adjusted with I_B, which will be carried out using a model-based design of a linear, time-invariant (LTI) output feedback control. Many AMB systems (with $I_B \geq I_c$) are controlled using PID control.[8,17] For complex AMB systems with multiple in- and outputs, $\mathcal{H}_\infty$-control[18–20] and μ-synthesis[20–25] are often used which allow for the inclusion of uncertainties and system limitations in the design. However, these designs often lead to high-order controllers and an order reduction technique has to be applied. To avoid this, the controller structure for the AMBs of the discussed test rig is fixed and only its parameters are optimized by minimizing the $\mathcal{H}_\infty$ norm of the system.[26] Comparable approaches for AMBs were used in References 27,28, utilizing more specialized objective functions and boundary condition formulations. However, the $\mathcal{H}_\infty$ norm allows easy adaptation and extension of the controller design. This approach also enables the inclusion of structured uncertainties in the design,[29] which will be used here to consider the speed-dependent eigenfrequencies of the flexible and gyroscopic rotor.

The model of the system is described and compared to measurements in Section 2. The focus here lies on the strong influence of the gyroscopic effects on the elastic rotor. Section 3 discusses the design of the controller and the simulated results for various I_B. An experimental investigation follows in Section 4.

2 | PLANT MODEL

The model of the plant has to contain all subsystems which have a major influence on the radial AMBs. This includes the AMBs and the rotor, but also the stator, the position sensors, the amplifier (AMP) of the AMBs and the PMSM. The latter has a negative radial stiffness due to the permanent magnets on the rotor. In this article, all subsystems are represented by linear, rational transfer functions (TFs). Models for the rotor and stator, which both have elastic eigenfrequencies in the speed range of the test rig, are discussed in Section 2.1. The AMBs and their AMP are described in Section 2.2. Section 2.3 gives an outline of the other subsystems and their connection in the overall plant model. A comparison between the derived model and experiments is shown in Section 2.4. A more detailed description of the model can be found in Reference 5.

2.1 | Rotor and stator

The rotor has four elastic eigenfrequencies below 500 Hz. Hence, its elasticity has to be considered in the model. To accomplish this, the rotor is modeled with cylindrical Timoshenko beam finite elements (cf. Reference 30) as shown in Figure 2. The outer part of the thrust disk, the permanent magnets of the PMSM, the shaft coupling, and the steel segments inside the FRP are modeled as masses without stiffness. The model has 74 elements and 75 nodes. Every node has four degrees of freedom x_i, y_i, $\varphi_{x,i}$, and $\varphi_{y,i}$, which describe the translational displacement in the radial x- and y-direction, as well as the rotation around the x- and y-axis, respectively. Ten nodes are highlighted in Figure 2. The red cross marks the node located in the center of gravity of the rotor. The translational displacement of nodes 1, 7, and 9 are measured by radial position sensors. The smallest air gaps between rotor and stator are at nodes 2 and 8, where touchdown bearings are located. The AMBs interact at nodes 3 and 6 and the PMSM at nodes 4 and 5.

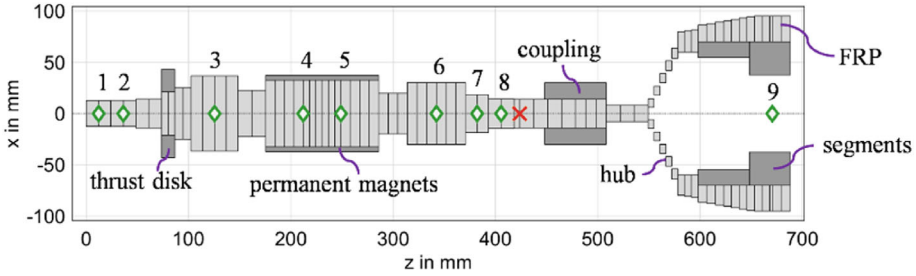

FIGURE 2 Beam finite element model of the rotor

Only linear material behavior and small deformations are considered in the beam finite element model (BFEM). Hence, a linear system of equations in the form of

$$\boldsymbol{M}\ddot{\boldsymbol{q}}_{\boldsymbol{r}} + (\boldsymbol{D} + \boldsymbol{G}(\Omega))\dot{\boldsymbol{q}}_{\boldsymbol{r}} + \boldsymbol{K}\boldsymbol{q}_{\boldsymbol{r}} = \boldsymbol{F}$$

$$\text{with} \quad \boldsymbol{q}_{\boldsymbol{r}} = \left[\ldots, x_i, \varphi_{y,i}, y_i, \varphi_{x,i}, \ldots \right]^{\mathrm{T}} \tag{1}$$

can be derived from the BFEM. $\boldsymbol{M}$, $\boldsymbol{D}$, and $\boldsymbol{K}$ are the mass, damping, and stiffness matrix, respectively. $\boldsymbol{G}(\Omega)$ is the gyroscopic matrix, which depends on the rotational frequency Ω. External forces on the rotor are summarized in the vector $\boldsymbol{F}$. $\boldsymbol{M}$, $\boldsymbol{K}$, and $\boldsymbol{G}(\Omega)$ are directly derived from the BFEM. $\boldsymbol{D}$ is estimated by means of modal damping factors, which are fitted to the measurements described in Section 2.4.

For a first validation of the BFEM, its eigenfrequencies are compared to the results of a volume finite element model (VFEM), which is implemented and evaluated in the commercial software *ANSYS Workbench*. For this comparison, the AMBs are simplified as springs with a constant stiffness of 10^6 N/m. The PMSM is neglected. The first four eigenmodes (EMs) of the VFEM sorted by ascending eigenfrequency (EF) at standstill are shown in Figure 3A. In this visual representation, red areas indicate large and blue areas small displacements. In the first EM, the rotor tilts around the PMSM and the upper AMB and the biggest displacement occurs at the specimen. The taper at the hub of the specimen shows a small elastic deformation. The second EM is characterized by translational movement of the rotor and tilting of the specimen around its center of gravity. All higher EMs show no or only a small movement of the center of gravity of the specimen. The fourth EM shows a clear elastic deformation of the rotor. The EFs of these EMs calculated for the BFEM and the VFEM are shown in Figure 3B under variation of Ω. Due to the gyroscopic effects, the EMs split into a forward mode, whose EF mostly increases with Ω, and a backward mode, whose EF decreases with Ω (cf. References 8,30). The EF of the first backward mode, which is about 16 Hz for $\Omega = 0$, approaches 0 Hz for high rotational speeds. In contrast, the EF of the fourth forward mode, which is about 400 Hz for $\Omega = 0$, rises to such an extent that, it is not equal to the rotational frequency below 40,000 rpm. The fifth and sixth EM, which are not shown in Figure 3, follow at 1 and 1.7 kHz and only show a small dependency on Ω. During acceleration, the forward modes of the first, second, and third EM have to be passed with the rotational speed to get to the operation range between 15,000 and 30,000 rpm. At these critical speeds, where Ω is equal to an EF of a forward mode, the unbalance of the rotor can lead to a strong excitation of the respective EM. The taper at the hub was designed so that no critical speed is inside the operation range.[5] The backward mode of the fourth EM, like all backward modes, does not get directly excited by the unbalance. The comparison between the BFEM and VFEM shows a good agreement. Hence, the BFEM, which has only 74 elements, compared to 228,695 elements in the VFEM, is used for the simulation of the rotor. To further decrease the calculation time for the following controller optimization, EMs with an EF above 5 kHz were removed from the rotor model since no influence of these EMs on the rotor's behavior has been observed in experiments.

The stator is also modeled with cylindrical beam finite elements, which are shown in Figure 4A. The marked nodes 1 to 9 are the counterparts of the respective nodes on the rotor. The red cross marks the center of gravity. The mass and the moment of inertia of the liner within the containment are lumped in node 10. Four spring elements are located at the corners of the base (see Figure 1) which support the test rig. Each spring has a horizontal stiffness $k_{\mathrm{mech},h}$ and a vertical stiffness $k_{\mathrm{mech},v}$. The distance between two springs along one side is l_{spring}. In the model, the springs are combined at node 11 to one translational spring with horizontal stiffness $4k_{\mathrm{mech},h}$ in x- and y-direction, respectively, and one rotational spring with stiffness $k_{\mathrm{mech},v}l^2_{\mathrm{spring}}$ around the x- and y-axis, respectively. The spindle housing is simplified as a homogenous

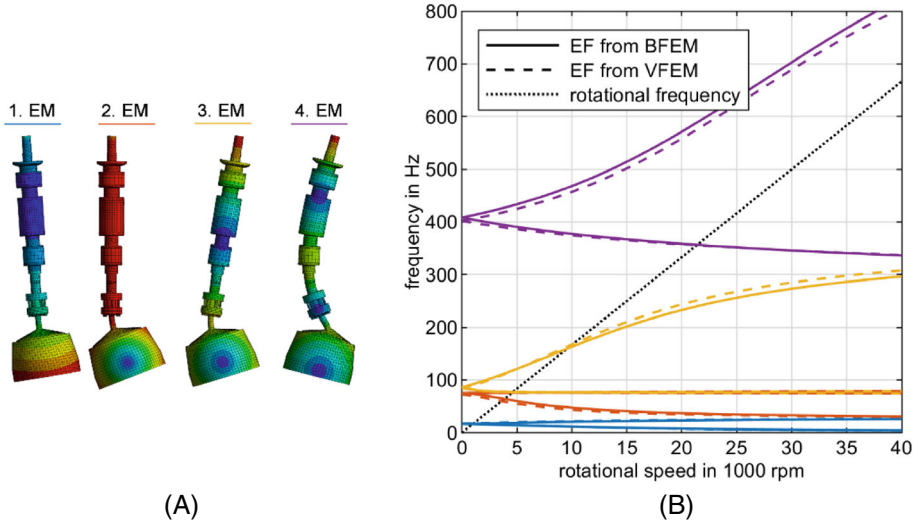

FIGURE 3 (A) Eigenmodes (EMs) of the rotor calculated by means of the volume finite element model (VFEM); (B) Comparison of the speed-dependent eigenfrequencies (EFs) calculated utilizing the beam finite element model (BFEM) and the VFEM. The line colors correspond to those shown in (A) above the EMs

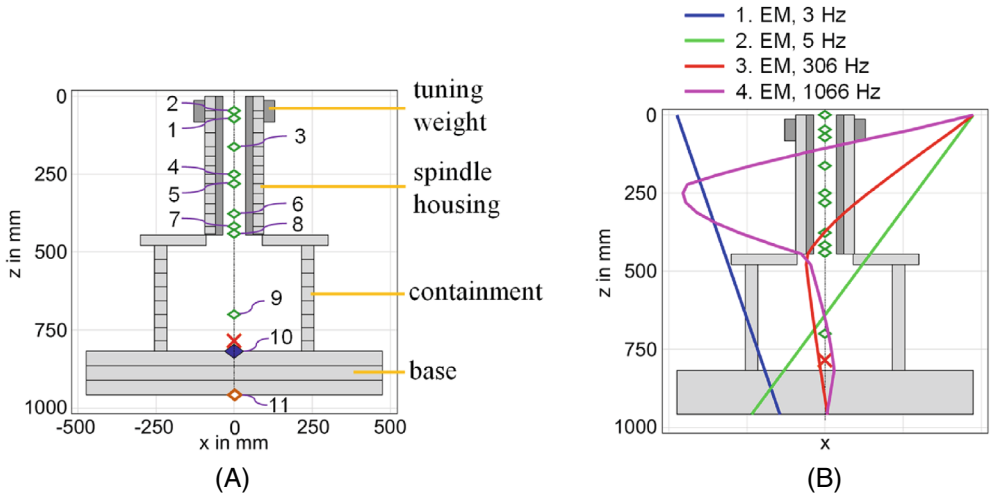

FIGURE 4 (A) Beam element model of the stator; (B) Calculated eigenmodes of the stator

cylinder. A stiffness-free mass on the inside of the housing is used to represent the actuators. The spindle housing has an additional supporting structure and a tuning weight, as can be seen in Figure A1. The stiffness of the support is included in the stiffness of the spindle housing and the tuning weight is modeled as a stiffness-free cylinder, which can be seen on the upper end of the stator in Figure 4.

A system of linear equations for the stator deflection $\boldsymbol{q_s}$ equivalent to Equation (1) can be derived from the BFEM. For the stator $\boldsymbol{G}(\Omega)$ is equal to $\mathbf{0}$ and the EMs and EFs are independent of the rotational speed of the rotor. The first four EMs of the stator are shown in Figure 4B. The first and second EM are rigid body modes of the stator on the spring elements. In the third and fourth EM, the spindle housing tilts on the lid of the containment. This behavior, which is known from measurements and a VFEM, is due to buckling of the lid and cannot be reproduced directly via beam elements. To create a similar behavior in the BFEM the modulus of elasticity of the lid was reduced to 0.075% of that of steel. The tuning weight and the supporting structure (see Figure A1) were introduced to reduce the vibration amplitudes when the third EM of the stator is excited. EMs higher in frequency than the fourth are poorly represented by the model and are therefore removed since no significant influence of these EMs on the behavior of the system was observed in experiments.

2.2 | Magnetic bearings

Both heteropolar radial AMBs have four pole pairs with a nominal radial air gap of 0.4 mm between rotor and stator. Two opposing pole pairs are operated together using a DWS for the x- and y-direction, respectively. In a DWS, separate coils are used for I_B and the control current I_c, which always has to be smaller than I_B.

The force of one AMB in one direction $F_{\mathrm{AMB},i}$ is approximated with the linearized equation

$$F_{\mathrm{AMB},i} = k_{I,i} I_{c,i} - k_{x,i}\, \Delta q_{\mathrm{AMB},i}, \tag{2}$$

where $\Delta q_{\mathrm{AMB},i}$ is the difference between the deflection of the rotor and the stator at the location of the AMB (cf. Reference 8). The proportionality factors $k_{I,i}$ and $k_{x,i}$ are calculated using a reluctance network of the AMB which is described in detail in Reference 5. Both depend on I_B, where $k_{I,i} \sim I_B$ and $k_{x,i} \sim I_B^2$. $k_{x,i}$ is negative, hence, $F_{\mathrm{AMB},i}$ increases with the relative deflection of the rotor. This unstable characteristic necessitates an active control of the AMBs. $F_{\mathrm{AMB},i}$ is adjusted by changing the voltage U_i applied to the control coil,[8] which in turn changes $I_{c,i}$. The resulting $I_{c,i}$ can be calculated with

$$U_i = R_i I_{c,i} + L_i \dot{I}_{c,i} + k_{\mathrm{ind},i} \Delta \dot{q}_{\mathrm{AMB},i}, \tag{3}$$

where R_i is the ohmic resistance and L_i the inductance of the control coil. The last term describes the induced voltage by the relative velocity of the rotor in the AMB $\Delta \dot{q}_{\mathrm{AMB},i}$. The factor $k_{\mathrm{ind},i}$ as well as L_i can be derived via the induction law and the reluctance network.[5] A more detailed discussion on AMBs can by be found in References 8,31.

U_i is adjusted by the AMP using pulse-width modulation with a main cycle frequency of 40 kHz. The control law, which determines the pulse-width for each main cycle, is implemented on a field programmable gate array (FPGA). For modeling purposes, it is assumed that the voltage pulses are perfectly rectangular. In this case, the duty cycle corresponds to the fraction of the average voltage of the present main cycle to the supply voltage. During one main cycle, the position and current signals are acquired, converted from analog to digital, the control law is evaluated and the voltage is applied to the coils. Data acquisition and conversion together take about 1 µs and the evaluation of the control law another 2 µs. This leaves around 22 µs per main cycle to adjust the voltage. Hence, the maximum mean voltage which can be applied to the coils is reduced from the voltage of the power supply of 54 V to 47.25 V. The discretization of the digital FPGA is neglected in the model and the output of the controller model is the analog set voltage U_{set}. The AMP is simulated as a time delay of 14 µs utilizing a third-order Padé approximant. The 14 µs result from the 3 µs for the data acquisition and evaluation plus half of the remaining main cycle time.

2.3 | Overall system

The sensors which are used to measure the radial position of the rotor have an external digital evaluation unit. It adds 14.3 µs of time delay to the system, which is again modeled using a third-order Padé approximant. The evaluation unit has an analog low pass filter (LP) with a cut-off frequency ω_c of 50 kHz and a digital LP with $\omega_c = 10$ kHz. After signal processing on the external evaluation unit, the signal is converted back to analog and passed on to the FPGA. The sensors used to monitor the position of the specimen can easily be damaged during operation, hence, they are not used to control the AMBs and are not included in the model. The current sensors have a cut-off frequency of 2 MHz. Their dynamic behavior is neglected in the model. All signals are filtered with an analog LP before the analog to digital conversion at the FPGA to reduce aliasing. This filter is a first order LP with a cut-off frequency of 5.6 kHz.

When the rotor is not centered in the stator, the magnets of the PMSM on the rotor create a radial force that pulls the rotor toward the stator. This force can be expressed via the negative stiffness $k_{x,\mathrm{PMSM}}$,[32] which can be estimated with

$$k_{x,\mathrm{PMSM}} = -\frac{\pi r_{P,\mathrm{PMSM}} l_{Fe,\mathrm{PMSM}} B_{L,\mathrm{PMSM}}^2}{2\mu_0 l_{L,\mathrm{PMSM}}}, \tag{4}$$

wherein μ_0 is the permeability of vacuum, $r_{P,\mathrm{PMSM}}$ the inner radius and $l_{Fe,\mathrm{PMSM}}$ the active length of the stator of the PMSM. $l_{L,\mathrm{PMSM}}$ is the length of its air gap. $B_{L,\mathrm{PMSM}}$ is the magnetic flux density in the air gap, which can be approximated with[33]

$$B_{L,\mathrm{PMSM}} = \frac{B_{R,\mathrm{Mag}}}{1 + \frac{l_{L,\mathrm{PMSM}} \mu_{r,\mathrm{Mag}}}{h_{\mathrm{Mag}}}}. \tag{5}$$

$B_{R,\mathrm{Mag}}$ is the remanent magnetization, $\mu_{r,\mathrm{Mag}}$ the relative permeability, and h_{Mag} the thickness of the permanent magnets. In the model, the radial force of the PMSM is evenly distributed between two nodes (see Section 2.1). The radial force on each node $F_{\mathrm{PMSM},i}$ results from

$$F_{\mathrm{PMSM},i} = -\frac{k_{x,\mathrm{PMSM}}}{2}\Delta q_{\mathrm{PMSM},i}, \tag{6}$$

where $\Delta q_{\mathrm{PMSM},i}$ is the relative deflection of the rotor at the respective nodes.

The overall model of the plant $\boldsymbol{\mathcal{P}}(s)$ is shown in Figure 5. The bold variables are vectors which group several variables, for example, $\boldsymbol{U}_{\mathrm{set}} = \left[U_{\mathrm{set},u,x}, U_{\mathrm{set},u,y}, U_{\mathrm{set},l,x}, U_{\mathrm{set},l,y}\right]^{\mathrm{T}}$ contains the set voltages for the control coil of the upper (index u) and lower (index l) AMB in x- and y-direction, respectively. In the following no distinction will be made between x and y due to the rotational symmetry of the model. The inputs of $\boldsymbol{\mathcal{P}}(s)$ are $\boldsymbol{F}_{\mathrm{un}}$ and $\boldsymbol{U}_{\mathrm{set}}$. $\boldsymbol{F}_{\mathrm{un}}$ contains rotational harmonic disturbance forces which are used to simulate the unbalance of the rotor. The outputs of $\boldsymbol{\mathcal{P}}(s)$ are $\Delta\boldsymbol{q}$, $\boldsymbol{I}_c$, $\Delta\tilde{\boldsymbol{q}}_{\mathrm{sen}}$, and $\tilde{\boldsymbol{I}}_c$. $\Delta\boldsymbol{q}$ is comprised of the relative rotor deflections ($\Delta\boldsymbol{q} = \boldsymbol{q}_r - \boldsymbol{q}_s$) at the touchdown bearings, the radial AMBs and the specimen (nodes 2, 3, 6, 8, and 9 in Figures 2 and 4A). $\Delta\tilde{\boldsymbol{q}}_{\mathrm{sen}}$ contains the measured and filtered relative rotor deflections (nodes 1 and 7 in Figures 2 and 4A) and $\tilde{\boldsymbol{I}}_c$ the filtered control currents.

2.4 | Experimental validation

To validate and adjust the model, measurements are performed on the test rig. For these measurements, the AMBs are controlled using a decentralized PID-controller for the position (cf. Reference 8) and a subordinate PI-controller for each current. The controller coefficients were adjusted experimentally.

First, the comparison between model and measurement is carried out using the diagonal elements $\mathcal{S}_{ii}(s)$ with $s \in \mathbb{C}$ of the sensitivity function $\boldsymbol{\mathcal{S}}(s)$ at $\Omega = 0$. The maximum gain of $\mathcal{S}_{ii}(j\omega)$ for $\omega \in \mathbb{R}$ and all i is a measure for the stability margins of the system.[34] Artificial noise n_i is added to the measured position signals $\Delta\tilde{q}_{\mathrm{sen},i}$ in the closed loop to acquire $\mathcal{S}_{ii}$ which is given by[34]

$$\mathcal{S}_{ii}(s) = \frac{\Delta\tilde{q}_{\mathrm{sen},i}(s) + n_i(s)}{n_i(s)}. \tag{7}$$

The measured and simulated $\mathcal{S}_{ii}$ of the system with $I_B = 4.3$ A is shown in Figure 6. The measurements with noise excitation showed a low coherence in the low-frequency range. Therefore, further measurements were performed in the low-frequency range using a mono-frequency sinusoidal excitation, which are marked with "x" and have a coherence of almost one. The model was adjusted to the measurement mainly by tuning the modal damping as well as the air gap of the AMBs and the PMSM.[5] The adjusted model shows good agreement with the measurement up to 1 kHz. However, the maximum gain of $\mathcal{S}_{ll}$ at the lower AMB is about 20 dB, which in the measurement can only be seen with the sinusoidal excitation. According to Reference 34, the gain should be below 12 dB to be suitable for long-term operation. This limit has to be considered in the following design of the controller.

To validate the model behavior with changing Ω, a slow acceleration from 0 to 30,000 rpm in approximately 300 s was recorded on the test rig. The measured deflections of the rotor and the specimen as well as the control currents

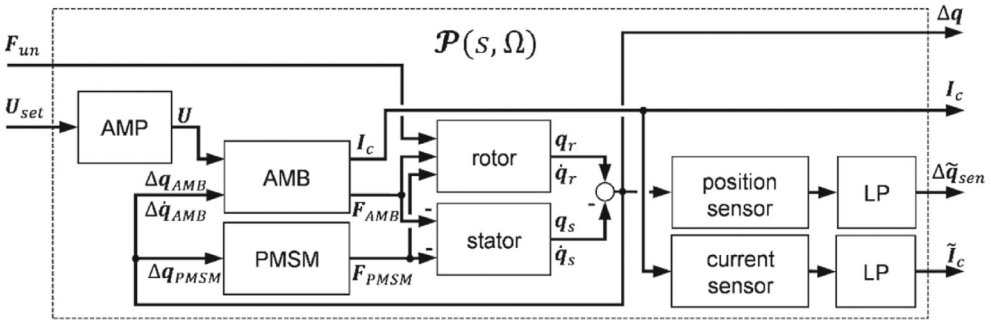

FIGURE 5 Structure of the plant model

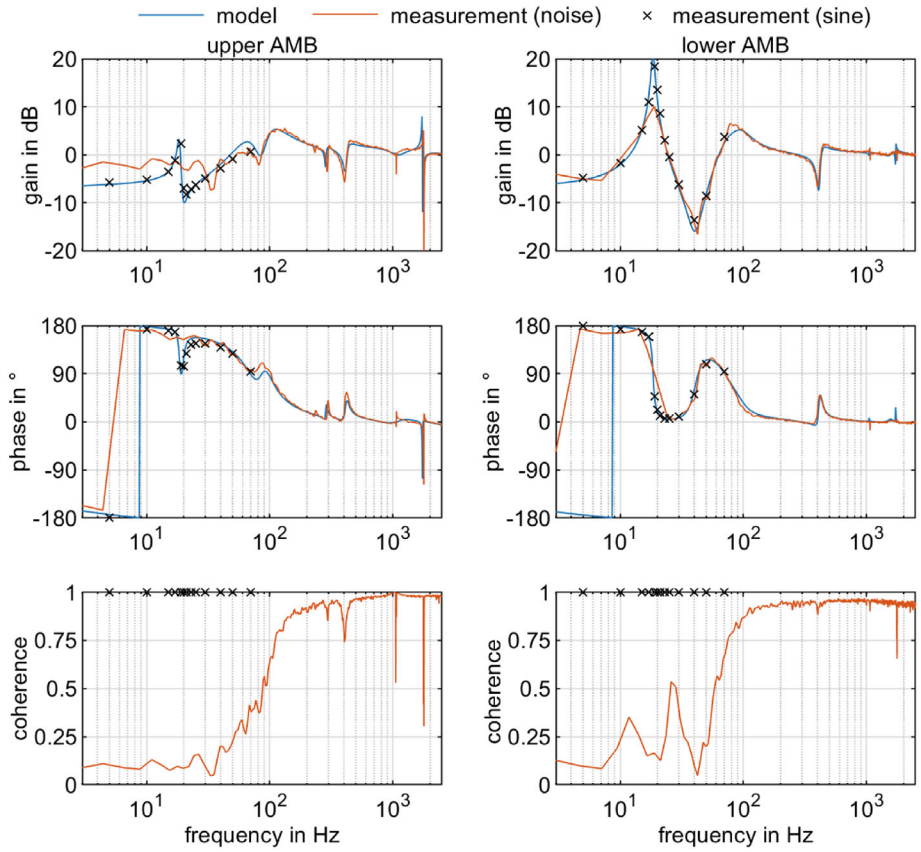

FIGURE 6 Simulated and measured diagonal elements of the sensitivity function of the AMBs at 0 rpm with a decentral PID control and $I_B = 4.3$ A. Two types of measurements were performed. The first using noise as excitation shows a low coherence below 100 Hz. Therefore, additional measurements with sinusoidal excitation were performed at low frequencies

of the upper and lower AMB are shown in Figure 7A. The first critical speed is passed at 1300 rpm, which results in comparatively high deflections at the lower measurement position and the specimen as well as high control currents in the lower radial AMB. For this reason, a high I_B of 7.6 A is used in the low speed range. Above 6000 rpm, I_B is reduced to 4.3 A and the amplification of the derivative term in the position controller is reduced by 36% so that the first backward mode, which approaches 0 Hz for high speeds, is not excited by amplified noise. To compare the rotor EFs of the model with the measurement, a measured Campbell diagram of the upper sensor is shown in Figure 7B. The yellow line going from 0 Hz at 0 rpm to 500 Hz at 30,000 rpm shows speed synchronous deflections, which dominate the deflections and reach 36 μm at 12,000 rpm. However, the amplitudes in the Campbell diagram are cut off at 1 μm in order to make the EFs visible. The other straight lines starting at 0 Hz are harmonic deflections of higher order. EFs are visible as blurry curved lines in the background. Dashed red lines show the calculated EFs from the model. The fourth EF is overestimated by the model by about 10 Hz. The increase of the EF of the third forward mode is underestimated. But in general, there is a good agreement between measurement and model.

3 | CONTROLLER DESIGN AND BIAS CURRENT REDUCTION

The derived model is used to design a controller for the system. At first, weighting functions for the physical inputs and outputs are introduced to incorporate performance and robustness goals in the design as well as to scale the TFs and make them dimensionless.[24] The $\mathcal{H}_\infty$ norm of the weighted TFs of the model will be used as the objective function for the controller optimization, which is described in the next section. Section 3.2 presents an approach to consider the strongly speed-dependent rotor behavior without making the design too conservative or requiring gain scheduling. This approach will be used to design controllers for the system with varying I_B, to determine how low I_B can be chosen (see Section 3.3).

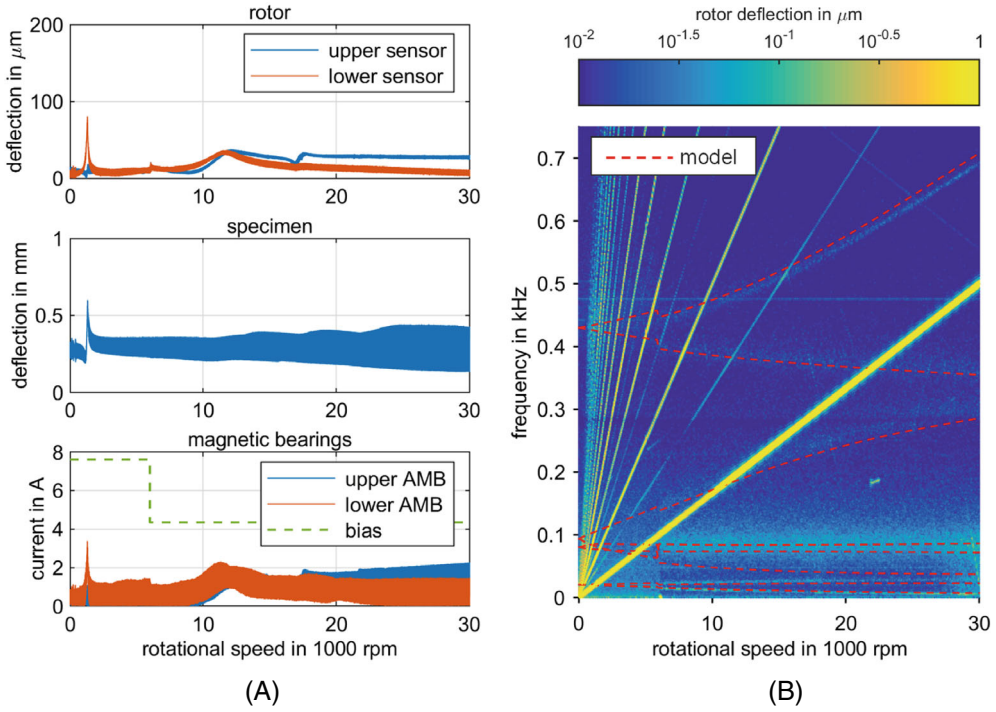

FIGURE 7 (A) Measured deflections and currents during acceleration from 0 to 30,000 rpm with a decentral PID control for the radial AMBs; (B) Campbell diagram of the rotor deflection at the upper radial position sensor. The shown deflection amplitudes in the Campbell diagram are cut off at 1 μm. The dashed red lines show the calculated eigenfrequencies of the rotor from the model

3.1 | Generalized model with weighted physical inputs

As described in Section 1, the goal of the controller design in this article is to find an LTI output feedback $\boldsymbol{C}(s)$ that stabilizes the plant and satisfies certain requirements. First, it is required that disturbances during operation must not lead to high relative rotor deflections, control currents or voltage demand. For this purpose, $\boldsymbol{\mathcal{P}}$ is extended to the weighted plant model $\boldsymbol{\mathcal{P}}_{\mathcal{W}}$ as shown in Figure 8. $\boldsymbol{U}_d$ and $\boldsymbol{n}$ are added as new inputs. $\boldsymbol{U}_d$ is a disturbance voltage which is added to the voltage $\boldsymbol{u}$ calculated by the controller. The sensor noise $\boldsymbol{n}$ is added to $\Delta\tilde{\boldsymbol{q}}_{\text{sen}}$ and $\tilde{\boldsymbol{I}}_c$, which are then combined to the measured plant output $\tilde{\boldsymbol{y}}$. The outputs $\Delta\boldsymbol{q}$ and $\boldsymbol{I}_c$ are used to evaluate the rotor deflections and control currents, respectively. Due to the simplified model of the AMP, only a phase shift occurs between $\boldsymbol{U}_{\text{set}}$ and $\boldsymbol{U}$. Since only the amplitude of the output signals will be utilized for the evaluation of the system, $\boldsymbol{U}_{\text{set}}$ could be used for the evaluation of the utilization of the voltage. However, since the TFs from $\boldsymbol{U}_d$ to $\boldsymbol{u}$ can be used to limit the influence of multiplicative model uncertainties[35] and $\boldsymbol{U}_d$ is usually small ($\boldsymbol{u} \approx \boldsymbol{U}_{\text{set}}$), $\boldsymbol{u}$ will be used here as the third evaluation output. Stable weighting functions $\boldsymbol{\mathcal{W}}$ are introduced for the disturbance inputs $\boldsymbol{F}_{un}$, $\boldsymbol{U}_d$, and $\boldsymbol{n}$ as well as the evaluation outputs $\Delta\boldsymbol{q}$, $\boldsymbol{I}_c$, and $\boldsymbol{u}$. Finally, the weighted disturbance inputs are combined in the vector $\boldsymbol{w}$ and the weighted evaluation outputs in the vector $\boldsymbol{z}$.

Since an LTI output feedback is used for the control of the AMBs, $\boldsymbol{u}$ is calculated from $\tilde{\boldsymbol{y}}$ with

$$\boldsymbol{u}(s) = -\boldsymbol{C}(s)\tilde{\boldsymbol{y}}(s). \tag{8}$$

$\boldsymbol{\mathcal{P}}_{\mathcal{W}}$ can be divided into four subsystems according to

$$\begin{bmatrix} \boldsymbol{z}(s) \\ \tilde{\boldsymbol{y}}(s) \end{bmatrix} = \underbrace{\begin{bmatrix} \boldsymbol{\mathcal{P}}_{zw}(s) & \boldsymbol{\mathcal{P}}_{zu}(s) \\ \boldsymbol{\mathcal{P}}_{\tilde{y}w}(s) & \boldsymbol{\mathcal{P}}_{\tilde{y}u}(s) \end{bmatrix}}_{\boldsymbol{\mathcal{P}}_{\mathcal{W}}(s)} \begin{bmatrix} \boldsymbol{w}(s) \\ \boldsymbol{u}(s) \end{bmatrix}. \tag{9}$$

Using Equations (8) and (9) yields the TF matrix

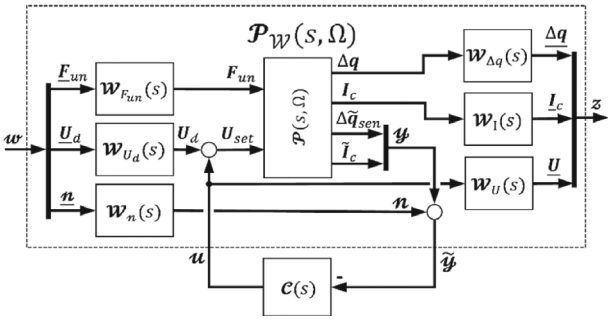

FIGURE 8 Weighted model of the plant with a controller

$$\mathcal{G}_{zw}(s) = \mathcal{P}_{zw}(s) - \mathcal{P}_{zu}(s)\mathcal{C}(s)\left(\mathcal{I} + \mathcal{P}_{\tilde{y}u}(s)\mathcal{C}(s)\right)^{-1}\mathcal{P}_{\tilde{y}w}(s) \tag{10}$$

from w to z. The goal of the controller design is to find the TF matrix $\mathcal{C}$ that stabilizes the closed loop and minimizes the influence of w on z. To quantify the latter, the $\mathcal{H}_\infty$ norm of the system $\|\mathcal{G}_{zw}(s)\|_\infty$ is used. The $\mathcal{H}_\infty$ norm of the rational transfer function matrix $\mathcal{G}$ is the supremum of the largest singular value $\overline{\sigma}$ of $\mathcal{G}$ over all frequencies $\omega \in \mathbb{R}$[35]

$$\|\mathcal{G}(s)\|_\infty = \sup_{\omega\in\mathbb{R}} \overline{\sigma}(\mathcal{G}(j\omega)). \tag{11}$$

The smallest $\|\mathcal{G}_{zw}(s)\|_\infty$ reached during the controller optimization, hence, the final value of the objective function of the optimization, will be denoted as γ. The weighting functions in $\mathcal{P}_{\mathcal{W}}$ are selected in such a way that all requirements on $\mathcal{G}_{zw}$ are fulfilled when $\|\mathcal{G}_{zw}(s)\|_\infty < 1$, hence, in the optimization when $\gamma < 1$.

To determine the weighting functions, first, physical limitations of the system are considered. For one thing, the relative rotor deflections at position i must not exceed the value $\Delta q_{\max,i}$. In particular, at positions 2 and 8 in Figures 2 and 4A the relative rotor deflections must not exceed the radial air gap of the touchdown bearings of $\Delta q_{\max,2} = \Delta q_{\max,8} = 0.2$ mm and at position 3 and 6 the radial air gap of the AMBs of $\Delta q_{\max,3} = \Delta q_{\max,6} = 0.4$ mm. Furthermore, the relative deflection of the specimen at position 9 must remain smaller than the radial air gap of its touchdown bearing of $\Delta q_{\max,9} = 2$ mm. Due to rotational symmetry, these limits apply to the x- as well as the y-direction. Hence, $\mathcal{W}_{\Delta q}$ is chosen as (cf. Reference 24)

$$\mathcal{W}_{\Delta q} = k_{\mathcal{W},\Delta q}\ \mathrm{diag}\left(q_{\max,2}^{-1}, q_{\max,2}^{-1}, \ \dots\ , q_{\max,9}^{-1}, q_{\max,9}^{-1}\right), \tag{12}$$

where $k_{\mathcal{W},\Delta q} = 1.25$ is a safety factor.

Similarly, $I_{c,i}$ must not surpass I_B and U_{set} cannot exceed $U_{\max}$. Since the model does not represent high frequencies well, the gain of their weighting functions $\mathcal{W}_I$ and $\mathcal{W}_U$ is increased for high frequencies to prevent high-frequency control activities.[22,23,36] With $\omega_{\mathcal{W},I,1} = \omega_{\mathcal{W},U,1} = 5$ kHz and $\omega_{\mathcal{W},I,2} = \omega_{\mathcal{W},U,2} = 500$ Hz, the weighting functions are chosen as

$$\begin{aligned} \mathcal{W}_I(s) &= k_{\mathcal{W},I} I_B^{-1} \frac{\left(s+\omega_{\mathcal{W},I,2}\right)\ \omega_{\mathcal{W},I,1}}{\left(s+\omega_{\mathcal{W},I,1}\right)\ \omega_{\mathcal{W},I,2}} \mathcal{I} \\ \text{and}\quad \mathcal{W}_U(s) &= k_{\mathcal{W},U} U_{\max}^{-1} \frac{\left(s+\omega_{\mathcal{W},U,2}\right)\ \omega_{\mathcal{W},U,1}}{\left(s+\omega_{\mathcal{W},U,1}\right)\ \omega_{\mathcal{W},U,2}} \mathcal{I}. \end{aligned} \tag{13}$$

$\mathcal{I}$ is an 4×4 identity matrix. $k_{\mathcal{W},I} = k_{\mathcal{W},U} = 1.6$ are introduced as safety factors.

The current noise input is scaled with the standard deviation of the measured current signals $n_{I,\max} = 1.2$ mA. $n_{I,\max}$ was measured while the current control was active (the AMP was switching) but the position control was deactivated. The position noise measured in the same manner would lead to a scaling factor of 0.4 μm. However, small scratches on the sensor target area on the rotor lead to further high-frequency excitation of the AMBs. These are one of the main reasons for the higher harmonic deflections in Figure 7B, which have a maximum amplitude of about 1 μm. To consider these scratches, the position noise input is scaled with $n_{\Delta q,\max} = 1\ \mu m$. The gain of the weighting functions is

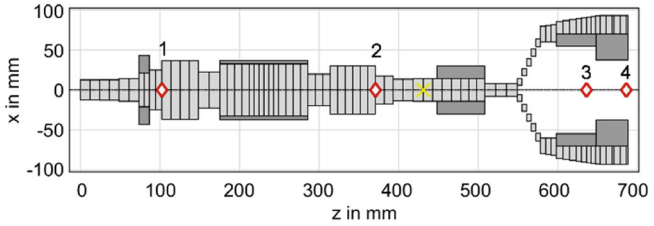

FIGURE 9 Unbalance of the rotor model

again increased for high frequencies to further reduce high-frequency control activities. The weighting functions are given by

$$\mathcal{W}_{n,I}(s) = n_{I,\max}\frac{3s + 3\omega_{\mathcal{W},n}}{s + 3\omega_{\mathcal{W},n}}\mathcal{I}$$
$$\text{and} \quad \mathcal{W}_{n,\Delta q}(s) = n_{\Delta q,\max}\frac{3s + 3\omega_{\mathcal{W},n}}{s + 3\omega_{\mathcal{W},n}}\mathcal{I} \tag{14}$$

with $\omega_{\mathcal{W},n} = 500$ Hz. $\boldsymbol{U}_d$ represents test signals which might be introduced to measure TFs.[20] But as mentioned before, this input can also be used to limit the susceptibility of the control to multiplicative model uncertainties. $\mathcal{W}_{U_d}$ is chosen as

$$\mathcal{W}_{U_d} = U_{d,\max}\,\mathcal{I} \tag{15}$$

with $U_{d,\max} = 0.1\ U_{\max}$.

Finally, the unbalance of the rotor is represented by external forces which are applied to the four discrete positions on the rotor shown in Figure 9. Test or compensation unbalance masses can be attached to these positions, allowing to experimentally identify the unbalance. The estimated unbalance $m_i\varepsilon_i$ is 3.6 gmm for position $i = 1$, 2.9 gmm for $i = 2$, 18.9 gmm for $i = 3$, and 16.3 gmm for $i = 4$. Note that with these four positions all four EMs shown in Figure 3A can be excited.

On each position i, the unbalance is represented by a force in x-direction $F_{\mathrm{Un},i,x}$ and a force in y-direction $F_{\mathrm{Un},i,y}$, so that the amplitude of the resulting force is equal to $m_i\varepsilon_i\Omega_j^2$ at a given speed Ω_j. In an idealized system, there is a 90° phase shift between $F_{\mathrm{Un},i,x}$ and $F_{\mathrm{Un},i,y}$ and each has an amplitude of $m_i\varepsilon_i\Omega_j^2$. For the controller design, $F_{\mathrm{Un},i,x}$ and $F_{\mathrm{Un},i,y}$ are modeled as distinct inputs, which results in the loss of the fixed phase relationship between them. Hence, the amplitudes of $F_{\mathrm{Un},i,x}$ and $F_{\mathrm{Un},i,y}$ are divided by $\sqrt{2}$ so that the maximum amplitude of the resulting force for any phase shift is still equal to $m_i\varepsilon_i\Omega_j^2$. Note that with this approach, the unbalance can directly excite the backward modes of the rotor model, which makes the controller design more conservative since this is not the case in the real system.

The excitation frequency of the unbalance is equal to the rotational speed. However, during the optimization all frequencies $\omega \in \mathbb{R}$ are checked (see Equation (11)). Hence, when the model is evaluated at a given speed Ω_j, a fourth-order bandpass filter is introduced in the weighting function of the unbalance, which attenuates the influence of non-rotor-synchronous frequencies. Finally, the weighting function of the unbalance inputs $\mathcal{W}_{F_{\mathrm{un}}}$ is given by

$$\mathcal{W}_{F_{\mathrm{un}}}(s,\Omega_j) = \frac{\left(0.02\ \Omega_j s\right)^4}{\left(s^2 + 0.02\ \Omega_j s + \Omega_j^2\right)^4}\frac{\Omega_j^2}{\sqrt{2}}\,\mathrm{diag}\left(m_1\varepsilon_1, m_1\varepsilon_1, \ \ldots\ , m_4\varepsilon_4, m_4\varepsilon_4\right). \tag{16}$$

3.2 | Approach for the controller design

When using $\mathcal{H}_\infty$ control theory, the controller which minimizes $\|\mathcal{G}_{\mathcal{z}w}\|_\infty$ normally has about the same order as $\mathcal{G}_{\mathcal{z}w}$.[35] Even if all EMs above 1 kHz are discarded in the model of the rotor, $\mathcal{P}$ still has an order of 92. The weighting functions further increase the order of the controller. The implementation of a controller of this order on the FPGA is not feasible. In this article, instead of reducing the controller after a $\mathcal{H}_\infty$ design process, the structure and thus the order of the

controller $\boldsymbol{C}$ is predefined and only the controller's parameters are adjusted using an optimization algorithm (cf. References 28,37). This procedure offers a wide range of possibilities for model-based tuning of the controller (cf. Reference 29), some of which will be utilized in the second part of this section. The parameter optimization will be performed using the function *hinfstruct* in *MATLAB*[26,38] which is based on Reference 39. This function first seeks parameters of $\boldsymbol{C}$ which stabilize the closed loop and then tries to minimize γ by adjusting the parameters. One disadvantage of *hinfstruct* is that it might converge to a local minimum, which makes it necessary to run the optimization several times with random start values. Furthermore, if the structure of $\boldsymbol{C}$ is poorly chosen, a stabilizing parameter set might not be found. However, it is already known from previous experiments that a cascaded decentral PID controller is sufficient to stabilize the examined system (see Section 2.4), which also gives a first set of stabilizing parameters as start values for one optimization run. In order to provide the optimization algorithm with more adjustment possibilities, the decentral PID-structure is extended with a PD-coupling of the position signals between the upper and lower AMB. The structure of the controller for one direction (x or y) is shown in Figure 10A. The decentral controller is shown in black, the coupling in green. Both PD- and PI-subsystems and additionally every D-term has an adjustable first order LP. Hence, 22 parameters can be adjusted during optimization. Negative and positive real values are allowed for the parameters of the P- and D-terms of the coupling controllers, all others are limited to positive real values. A minimum value is defined for the I-parameters to lift the rotor out of the touchdown bearings. The minimum value of the LP cut-off frequency is set to 10 Hz. Due to the vertical orientation and the rotational symmetry of the test rig, the same parameter set is used for the x- and y-direction. A coupling between the x- and y-direction in the controller is not considered in this article.

As an example, a controller is designed for the generalized plant model from Section 3.1 with $I_B = 4.3$ A and $\Omega = 375$ Hz, which is in the middle of the operational speed range, using *hinfstruct* and the coupled PID-controller structure (Figure 10A). After four optimization runs with different initial parameters, the best controller reached $\gamma = 0.37$. Hence, for $\Omega = 375$ Hz all requirements so far are met. However, this is not the case if Ω changes. This can be seen in Figure 10B, in which $\|\boldsymbol{\mathcal{G}}_{zw}(s,\Omega_i)\|_\infty$ with the optimized controller is evaluated at 300 equally distributed Ω_i in the speed range $\Omega_{\text{ges}} =$ [0 Hz, 500 Hz]. At 22,500 rpm $\|\boldsymbol{\mathcal{G}}_{zw}(s,\Omega_i)\|_\infty$ approximately equals γ, but between 8000 and 13,000 rpm $\|\boldsymbol{\mathcal{G}}_{zw}(s,\Omega_i)\|_\infty$ exceeds one and reaches 128. Hence, the controller does not meet the criteria imposed by the weighting functions in this speed range.

Another aspect which has to be checked, is the sensitivity of the system, hence, the maximum gain of $S_{ii}(s,\Omega)$ for all $s \in \mathbb{C}$ and $\Omega \in \Omega_{\text{ges}}$ has to be determined. Since $S_{ii}(s,\Omega)$ is a single-input-single-output (SISO) TF, finding its maximum gain over all $s \in \mathbb{C}$ for a given Ω_j is equivalent to the evaluation of $\left\|S_{ii}(s,\Omega_j)\right\|_\infty$. The maximum gain for all $\Omega \in \Omega_{\text{ges}}$ is approximated by calculating $\|S_{ii}(s,\Omega_i)\|_\infty$ at 300 equally distributed Ω_i in Ω_{ges}. $\|S_{ii}(s,\Omega)\|_\infty$ has to be computed for both bearings. The sensitivity $\|S_{uu}(s,\Omega_i)\|_\infty$ of the upper AMB (in x- or y-direction) and the sensitivity $\|S_{ll}(s,\Omega_i)\|_\infty$ of the lower AMB (in x- or y-direction) are shown in Figure 10B divided by $10^{0.6}$ (12 dB). As mentioned in Section 2.4, the gain of

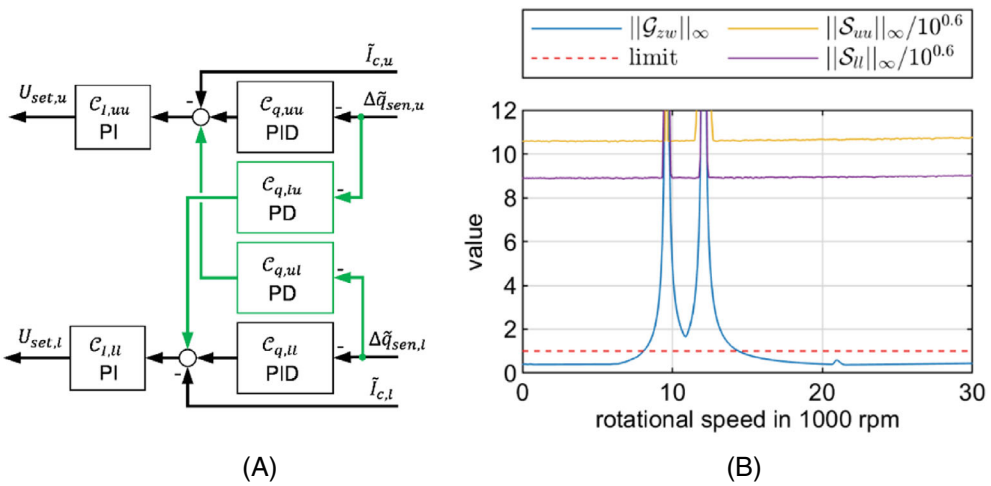

FIGURE 10 (A) Structure of the controller in one radial direction. The decentral controller is shown in black, the added coupling in green; (B) Largest singular value over the rotational speed of the controlled system with $I_B = 4.3$ A and the controller designed for $\Omega = 375$ Hz (22,500 rpm)

all S_{ii} should be below 12 dB. However, as can be seen in Figure 10B, even at the design speed of 22,500 rpm, $\|S_{uu}(s,\Omega_i)\|_\infty$ exceeds this limit by a factor of 10 and $\|S_{ll}(s,\Omega_i)\|_\infty$ exceeds it by a factor of eight.

Hence, the sensitivity function matrix $\boldsymbol{S}$ as well as the speed-dependent dynamics of $\boldsymbol{P}$ must be considered in the design of the controller. There are several ways to achieve the latter. The controller can be designed for different rotational speeds Ω_j and then switched or interpolated when Ω changes (e.g., Reference 40). Alternatively, the model uncertainty could be considered as further TFs in $\boldsymbol{P}_\mathcal{W}$, which might lead to very conservative results. The approach that will be taken in this article is to tune the controller for multiple Ω_j simultaneously. To accomplish this, several TFs of the plant at different Ω_j are connected in parallel. For example, for two rotational speeds Ω_1 and Ω_2 Equation (9) turns into

$$\begin{bmatrix} \boldsymbol{z}_1(s) \\ \tilde{\boldsymbol{y}}_1(s) \\ \boldsymbol{z}_2(s) \\ \tilde{\boldsymbol{y}}_2(s) \end{bmatrix} = \begin{bmatrix} \boldsymbol{P}_{zw}(s,\Omega_1) & \boldsymbol{P}_{zu}(s,\Omega_1) & \boldsymbol{0} & \boldsymbol{0} \\ \boldsymbol{P}_{\tilde{y}w}(s,\Omega_1) & \boldsymbol{P}_{\tilde{y}u}(s,\Omega_1) & \boldsymbol{0} & \boldsymbol{0} \\ \boldsymbol{0} & \boldsymbol{0} & \boldsymbol{P}_{zw}(s,\Omega_2) & \boldsymbol{P}_{zu}(s,\Omega_2) \\ \boldsymbol{0} & \boldsymbol{0} & \boldsymbol{P}_{\tilde{y}w}(s,\Omega_2) & \boldsymbol{P}_{\tilde{y}u}(s,\Omega_2) \end{bmatrix} \begin{bmatrix} \boldsymbol{w}_1(s) \\ \boldsymbol{u}_1(s) \\ \boldsymbol{w}_2(s) \\ \boldsymbol{u}_2(s) \end{bmatrix}. \tag{17}$$

In the same manner, the controller from Equation (8) gets expanded to (cf. Reference 26)

$$\begin{bmatrix} \boldsymbol{u}_1(s) \\ \boldsymbol{u}_2(s) \end{bmatrix} = \begin{bmatrix} -\boldsymbol{C}(s) & \boldsymbol{0} \\ \boldsymbol{0} & -\boldsymbol{C}(s) \end{bmatrix} \begin{bmatrix} \tilde{\boldsymbol{y}}_1(s) \\ \tilde{\boldsymbol{y}}_2(s) \end{bmatrix}. \tag{18}$$

Note that the parameterization of $\boldsymbol{C}$ for both subsystems is the same. This is possible since a parameter in the optimization with *hinfstruct* can be used at multiple positions. The goal of the optimization becomes

$$\min_{\boldsymbol{C}(s)} \left\| \mathrm{diag}\left(\boldsymbol{G}_{\boldsymbol{z}w}(s,\Omega_1), \boldsymbol{G}_{\boldsymbol{z}w}(s,\Omega_2)\right) \right\|_\infty, \tag{19}$$

which will minimize the maximum of the $\mathcal{H}_\infty$ norms of both systems.[26] If the $\mathcal{H}_\infty$ norm in Equation (19) is less than one, both systems meet the design criteria. This can be extended accordingly for any number of Ω_j. However, it must be considered that the computational effort for the controller design increases significantly with each new subsystem, even if the order of the controller $\boldsymbol{C}$ remains the same. Therefore, only as many subsystems as necessary should be used.

As previously mentioned, the controller design should also consider the 12 dB-limit on S_{ii}. This constrained could be addressed by including $\tilde{\boldsymbol{y}}$ in $\boldsymbol{z}$ (see Figure 8), since the TFs from $\boldsymbol{n}$ to $\tilde{\boldsymbol{y}}$ correspond to $\boldsymbol{S}$. However, to incorporate the 12 dB requirement on $\boldsymbol{S}$ from Reference 34, noise with an amplitude 40 times higher than the measured one would have to be considered. This approach would lead to an undesirably conservative controller design, as $\boldsymbol{n}$ also excites the other outputs of $\boldsymbol{P}_\mathcal{W}$. Therefore, another system $\boldsymbol{P}_{\mathcal{W},S}$ is set up which only includes the inputs and outputs needed for $\boldsymbol{S}$ as well as a weighting function $\boldsymbol{\mathcal{W}}_S$. The system is shown in Figure 11A. The input $\boldsymbol{n}_{\Delta q}$ is noise which is added to the position signals. The output is

$$\tilde{\boldsymbol{y}}_{\Delta q} = \Delta\tilde{\boldsymbol{q}}_{\mathrm{sen}} + \boldsymbol{n}_{\Delta q}. \tag{20}$$

The weighting function is chosen as

$$\boldsymbol{\mathcal{W}}_S(s) = 10^{-0.6}\frac{s+\omega_{S,2}}{s+\omega_{S,1}}\,\boldsymbol{\mathcal{I}} \tag{21}$$

with $\omega_{S,1} = 1$ mHz and $\omega_{S,2} = 1.5$ Hz. The LP in Equation (21) is introduced to achieve a good tracking behavior at low frequencies[20] and, more importantly for this test rig, to prevent the first backward EM of the rotor from moving to very low frequencies at high speeds. Note that also the off-diagonal elements of $\boldsymbol{S}$ are included in the design, which is not necessary according to Reference 34 and can be avoided by further splitting $\boldsymbol{S}$ in S_{uu} and S_{ll}. However, the latter might lead to high amplitudes of the off-diagonal elements of $\boldsymbol{S}$, which should be considered here, especially because of the optimization of the coupling subsystems in the controller. As a compromise, the full TF matrix $\boldsymbol{S}$ will be included in the controller optimization, but it will only be checked for S_{ii} if they also meet the criteria for other $\Omega \in \Omega_{\mathrm{ges}}$. Hence, after a successful controller optimization, $\|\boldsymbol{\mathcal{W}}_S(s)\boldsymbol{S}(s,\Omega)\|_\infty$ will be smaller than one for the Ω_j which were included in the

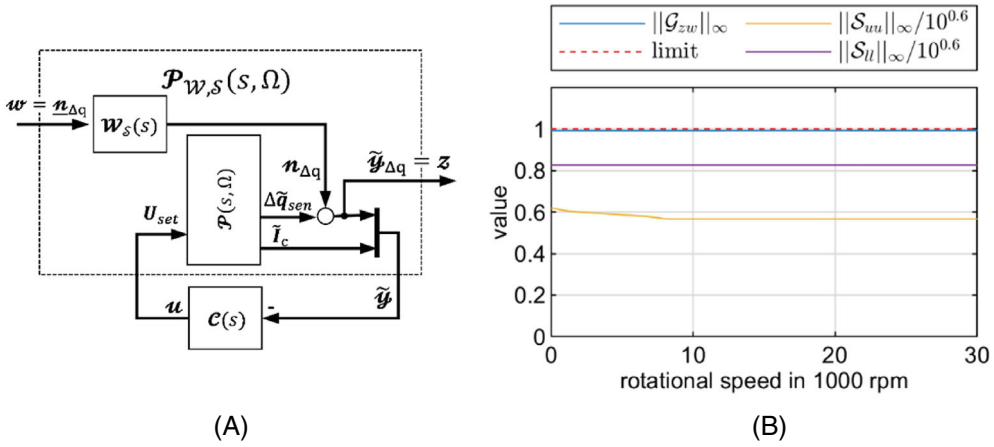

FIGURE 11 (A) Weighted model of the sensitivity function; (B) Largest singular value of the controlled generalized model and the diagonal elements of the weighted sensitivity function over the rotational speed with $I_B = 4.3$ A where the controller is designed for multiple systems $\mathcal{G}_{zw}(s,\Omega_j)$ and $\mathcal{W}_S(s)\mathcal{S}(s,\Omega_j)$ for various rotational speeds Ω_j.

design process, but might exceed one at deviating Ω. In the designed controllers discussed in the following section, the computed values of $\|\mathcal{W}_S(s)\mathcal{S}(s,\Omega_i)\|_\infty$ never exceeded 1.6 and only exceeded 1.2 for $I_B > 4.6$ A. Applying the 12 dB limit to the full TF matrix $\mathcal{S}$ implies that the maximum gain of S_{ii} is smaller than 12 dB, hence, the design could be seen as conservative. However, this is intended here since new systems should rather aim at a value of 9.5 dB.[34] For future work, it will be useful to determine a valid limit for $\|\mathcal{S}\|_\infty$ or to check if the 12 dB limit (or 9.5 dB limit) should be applied to the off-diagonal elements of $\mathcal{S}$ as well.

Like $\mathcal{G}_{zw}$, $\mathcal{S}$ will generally have to be considered in the controller design for multiple Ω_j. Hence, the goal of the optimization now is

$$\min_{C(s)} \|\mathrm{diag}\left(\mathcal{G}_{zw}(s,\Omega_1),\ \dots\ ,\mathcal{G}_{zw}(s,\Omega_n),\mathcal{W}_S(s)\mathcal{S}(s,\Omega_{n+1}),\ \dots\ ,\mathcal{W}_S(s)\mathcal{S}(s,\Omega_m)\right)\|_\infty . \tag{22}$$

An iterative process is used to determine which $\mathcal{G}_{zw}(s,\Omega_j)$ and $\mathcal{S}(s,\Omega_j)$ have to be included in Equation (22). For example, continuing from Figure 10B, a next step could be to include $\mathcal{G}_{zw}$ and $\mathcal{S}$ for 9700 rpm to counteract the first distinct peak in $\|\mathcal{G}_{zw}(s,\Omega_i)\|_\infty$ and then rerun the controller optimization. Afterwards, $\|\mathcal{G}_{zw}(s,\Omega)\|_\infty$ and $\left\|\mathcal{W}_{S,ii}(s)\mathcal{S}_{ii}(s,\Omega)\right\|_\infty$ are evaluated again with the new controller parameters for all $\Omega \in \Omega_{\mathrm{ges}}$. To formalize the procedure, the values $\Gamma_{\max}$ and $\Gamma_{\min}$ of the TFs are determined where

$$\Gamma_{\max} = \max_{\Omega \text{ in } \Omega_{ges}} (\Gamma(\Omega)),$$

$$\text{and} \quad \Gamma_{\min} = \min_{\Omega \text{ in } \Omega_{ges}} (\Gamma(\Omega))$$

$$\text{with} \quad \Gamma(\Omega) = \max\left(\|\mathcal{G}_{zw}(s,\Omega)\|_\infty, \left\|\mathcal{W}_{S,ii}(s)\mathcal{S}_{ii}(s,\Omega)\right\|_\infty\right). \tag{23}$$

If $\Gamma_{\max} \leq 1$, the designed controller can be used and the design process is finished. If $\Gamma_{\min} > 1$, the present controller cannot be used for the system. Hence, either the system cannot be robustly stabilized with the predefined controller structure or the optimization has to be repeated with different starting parameters, since it cannot determine if it reached the global minimum. However, if $\Gamma_{\max} > 1$ and $\Gamma_{\min} < 1$, hence, $\|\mathcal{G}_{zw}(s,\Omega)\|_\infty$ or $\left\|\mathcal{W}_{S,ii}(s)\mathcal{S}_{ii}(s,\Omega)\right\|_\infty$ is below one for some $\Omega \in \Omega_{\mathrm{ges}}$ and above one for others, $\mathcal{G}_{zw}(s,\Omega_j)$ or $\mathcal{S}(s,\Omega_j)$, respectively, has to be included in Equation (22) for a Ω_j in the area where it is above one. After the subsequent controller optimization, $\Gamma_{\max}$ and $\Gamma_{\min}$ have to be evaluated again. This procedure is repeated until either $\Gamma_{\max} \leq 1$ or $\Gamma_{\min} > 1$.

For this article, $\mathcal{G}_{zw}(s,\Omega_j)$ and $\mathcal{S}(s,\Omega_j)$ were chosen in such away, that $\Gamma_{\max}$ and $\Gamma_{\min}$ are not only both above or below one, but $\Gamma(\Omega)$ is approximately constant and equal to γ for all $\Omega \in \Omega_{\mathrm{ges}}$, hence $\Gamma_{\max} \approx \Gamma_{\min} \approx \gamma$. In other words, the controller performance is almost independent of Ω, simplifying the performance comparison of the optimized controllers for different I_B by means of γ.

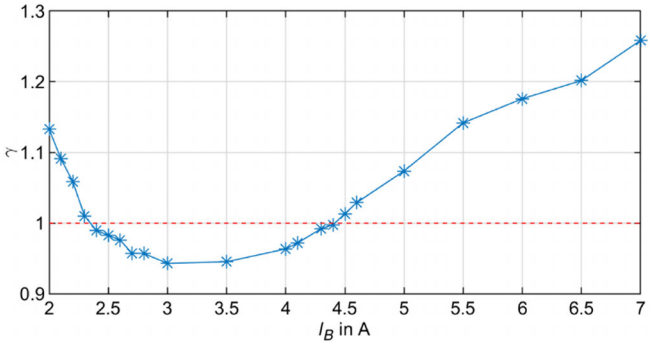

FIGURE 12 Smallest γ which was reached by the parameter optimization of a predefined controller for the system with different I_B where the controller performance is nearly independent of Ω for 300 tested Ω_i in Ω_{ges}

For the test rig with $I_B = 4.3$ A, $\boldsymbol{\mathcal{G}}_{\boldsymbol{\varkappa w}}(s, \Omega_j)$ was included in the controller design for 0, 9700, 21,500, and 31,000 rpm and $\boldsymbol{\mathcal{W}}_S(s)\boldsymbol{\mathcal{S}}(s, \Omega_j)$ for 0, 5500, 9700, and 31,000 rpm. Thirty one thousand rpm was included to ensure AMB stability in the case the PMSM control overshoots 30,000 rpm. The smallest γ which was reached after four optimization runs was 0.99. Compared to the previous optimization, γ increased since the design is now more restrictive. However, $\Gamma(\Omega)$ is nearly constant over Ω. This can be seen in Figure 11B, in which $\|\boldsymbol{\mathcal{G}}_{\boldsymbol{\varkappa w}}(s, \Omega_i)\|_\infty$, $\|S_{uu}(s, \Omega_i)\|_\infty / 10^{0.6}$, and $\|S_{ll}(s, \Omega_i)\|_\infty / 10^{0.6}$ are shown for the system with the optimized controller. The values are again evaluated at 300 equally distributed Ω_i in Ω_{ges}. Between 0 and 30,000 rpm $\|\boldsymbol{\mathcal{G}}_{\boldsymbol{\varkappa w}}(s, \Omega_i)\|_\infty$, which here is bigger than the other two, is always smaller than one and deviates from γ only by 0.06%. $\|S_{uu}(s, \Omega_i)\|_\infty$ and $\|S_{ll}(s, \Omega_i)\|_\infty$ are also below $10^{0.6}$ for all evaluated Ω_i. Hence, the derived controller meets all design criteria.

3.3 | Minimum bias current

The previously described controller design process was repeated for several I_B with a minimum step size of 0.1 A to approximate the smallest I_B for which a permissible controller can be found. Ω_j for which $\boldsymbol{\mathcal{G}}_{\boldsymbol{\varkappa w}}$ and $\boldsymbol{\mathcal{S}}$ have to be included in the design generally change with I_B and have to be adjusted accordingly. More Ω_j had to be included in the design for small I_B ($I_B < 2.5$ A) than for bigger I_B. The smallest γ obtained for each I_B is shown in Figure 12. The maximum deviation from $\Gamma(\Omega_i)$ to γ is less than 0.4%, again evaluated at 300 equally distributed Ω_i in Ω_{ges}. More importantly, if $\gamma \leq 1$, then $\Gamma_{\max} \leq 1$ and if $\gamma > 1$, then $\Gamma_{\min} > 1$. The smallest calculated γ is at $I_B = 3$ A. From here, γ rises for increasing and decreasing I_B. The smallest I_B with $\gamma \leq 1$ is 2.4 A. Hence, 2.4 A is the smallest I_B for which a controller of the predefined structure was found with which the closed loop meets the criteria defined by the weighted TFs. In contrast, the highest I_B for which a permissible controller was found is 4.4 A.

For all I_B, the weighted TFs with the highest gain, therefore the ones which dominate the design process, are $\mathcal{W}_{S,ii}S_{ii}$ at small frequencies (10–100 Hz) and the TFs $\boldsymbol{\mathcal{G}}_{\underline{\boldsymbol{U}}\,\underline{\boldsymbol{n}}}$ from $\underline{\boldsymbol{n}}$ to $\underline{\boldsymbol{U}}$ (see Figure 8) at high frequencies (>1 kHz). For small I_B, the weighted TFs from all disturbance inputs $\boldsymbol{w}$ to the weighted control currents $\underline{\boldsymbol{I}}_C$ also become significant as the control currents are restricted by I_B (see Equation 13). This is particularly pronounced in the low-frequency range (< 100 Hz). An adjustment of the controller to avoid current saturation leads to an increase of the high-frequency gain of $\boldsymbol{\mathcal{G}}_{\underline{\boldsymbol{U}}\,\underline{\boldsymbol{n}}}$. This trade-off as well as the reduced maximum force and the smaller force slew rate leads to an increase of γ for small I_B. The increase of γ for high I_B can be attributed to the enlarged negative stiffness of the AMBs (see Equation 2), which has to be compensated by an increased feedback gain. This in turn amplifies the susceptibility to noise. If one AMB is simplified as a SISO system, the growth of γ with I_B can more formally be explained by the increase of the value of Bode's sensitivity integral,[35,41] since the real part of the unstable poles of the open loop rise with I_B. Hence, the gain of the sensitivity function has to increase with I_B in some frequency range. The assumption of a SISO system is of course not accurate here since the upper and lower AMB are coupled in the controller and by the rotor, among other things, but a comparable behavior is also to be expected for multiple-input-multiple-output systems (cf. Reference 42).

A qualitative description of how the parameters of the optimized controllers change with I_B is given in Appendix B. Experimental validations of some of the controllers as well as the reduction of the rotor temperature are shown in the next section.

4 | EXPERIMENTAL VALIDATION

At first, the sensitivity of the system with an optimized controller is evaluated. The gain of the sensitivity function at 0 rpm of the upper and lower AMB with $I_B = 2.4$ A and the respective optimized controller are shown in Figure 13. Simulated as well as measured results with noise excitation and sinusoidal excitation are shown. Slight deviations are evident between the model and the measurements, but the maximum gain is below the required 12 dB and even below 9.5 dB (see Section 3.2). The same is true for the sensitivity functions of both AMBs with $I_B = 4.3$ A and the respective optimized controller (see Figure A2). Hence, a significant reduction of the sensitivity in comparison to the previous experimentally adjusted decentral PID controller was achieved (cf. Figure 6).

In a next step, the optimized controllers for the AMBs with $I_B = 2.4$ A, $I_B = 2.6$ A, $I_B = 3.0$ A, and $I_B = 4.0$ A are tested during an acceleration of the rotor with the specimen from 0 to 30,000 rpm. The measured deflections of the rotor as well as the currents of the radial AMBs are shown in Figure 14. The deflections of the specimen are shown in Figure A3, which look almost identical in all four measurements. In comparison to the decentral PID controller (see Figure 7A), the optimized controllers show a smaller influence of high-frequency disturbances, which can be seen in the current plots. Furthermore, the deflections and currents while passing the first EF of the rotor with the optimized controllers are considerably smaller than with the decentral PID controller, whereas they are higher while passing the third EF of the rotor. Especially for $I_B = 2.4$ A and $I_B = 4.0$ A, the control currents get close to I_B around the third EF. This might be due to an underestimation of the unbalance of this EM in the model. The measurement with $I_B = 2.6$ A shows the smallest deflections and currents. The rotational speed at which the first and third EF are passed increases from 650 rpm with $I_B = 2.4$ A to 800 rpm with $I_B = 4.0$ A and from 9000 rpm with $I_B = 2.4$ A to 10,400 rpm with $I_B = 4.0$ A, respectively. Furthermore, with increasing I_B also increases the excitation of the stator-EF at 17,000 rpm. However, all four controllers can be used in the entire speed range and all have a smaller gain of the sensitivity function than the decentral PID controller.

To evaluate the influence of I_B on the rotor temperature, further measurements are performed where, after an initial acceleration to 15,000 rpm, the rotor with the specimen was periodically accelerated until the rotor reached a temperature of around 94°C. Each acceleration cycle consists of an acceleration from 15,000 to 30,000 rpm in 10 s, a hold time $t_{30k} = 2$ s at 30,000 rpm, a deceleration to 15,000 rpm in 10 s and a hold time $t_{15k} = 2$ s at 15,000 rpm. Then the cycle repeats. t_{30k} and t_{15k} are used to let the rotational speed settle. The rotor temperature is measured contactless with two infrared sensors. The upper sensor measures the temperature between the thrust disk of the axial AMB and the upper radial AMB, the lower sensor measures below the lower radial AMB at the same axial position as the lower radial position sensors

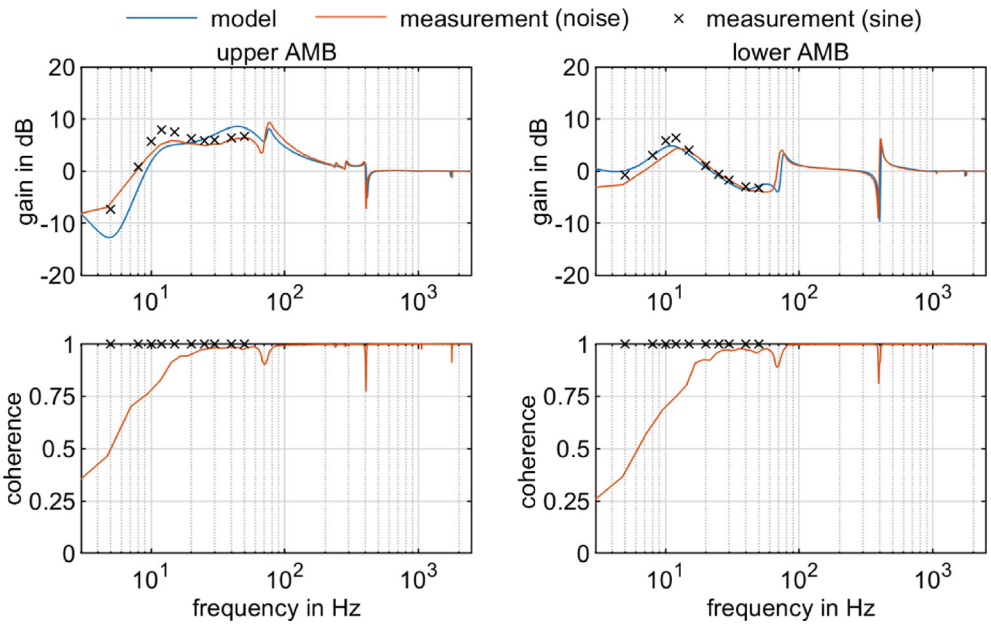

FIGURE 13 Simulated and measured diagonal elements of the sensitivity function of the AMBs at 0 rpm with $I_B = 2.4$ A and the respective optimized controller. The measurements were performed using noise and sinusoidal excitation

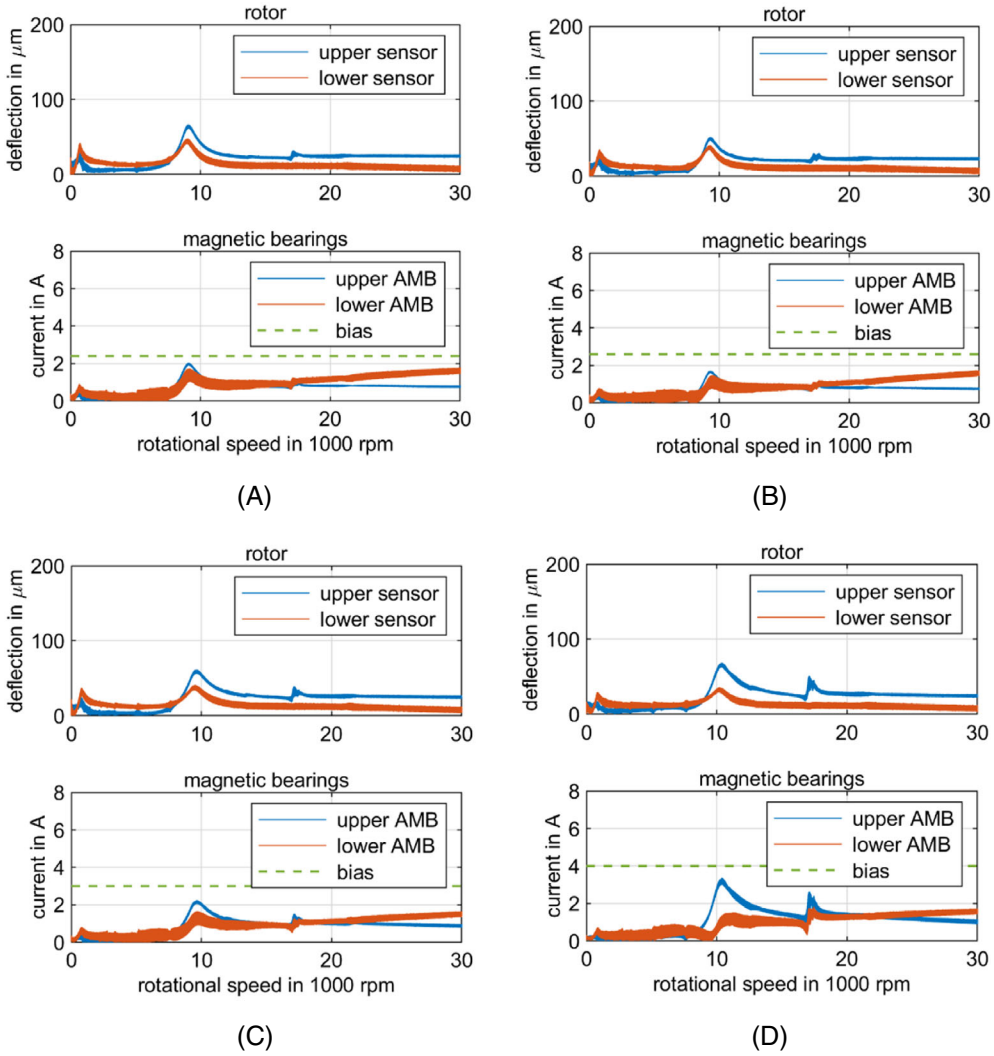

FIGURE 14 Measured rotor deflection and currents during an acceleration from 0 to 30,000 rpm in 300 s with (A) $I_B = 2.4$ A, (B) $I_B = 2.6$ A, (C) $I_B = 3.0$ A, and (D) $I_B = 4.0$ A and the respective optimized controller

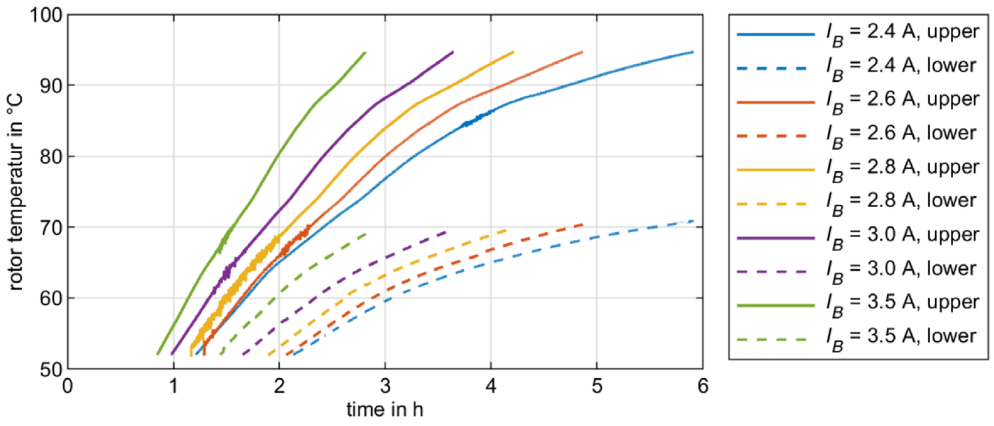

FIGURE 15 Measured rotor temperature at the upper and lower measurement position during cycling with different bias currents

(see Figure 1). The measured rotor temperatures at these positions during cycling with different I_B are shown in Figure 15. The used sensors can only measure temperatures above 50°C. At the start of each measurement, the test stand was at the ambient temperature of about 20°C.

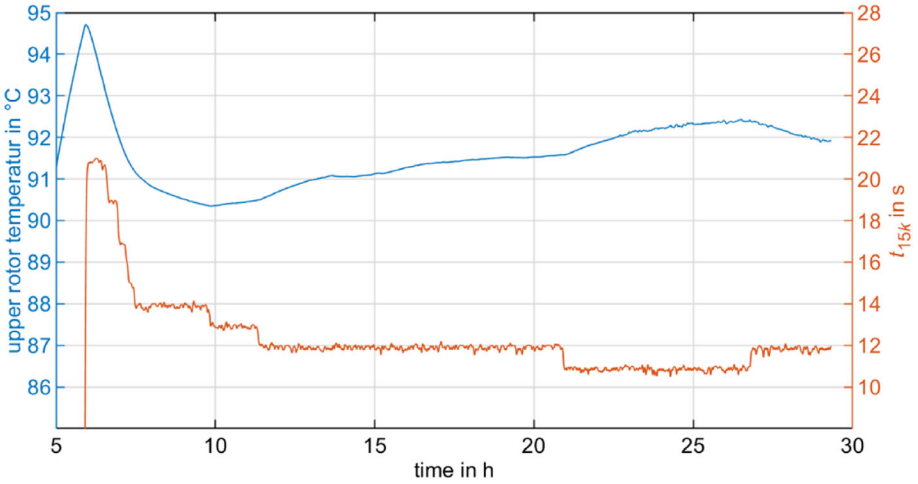

FIGURE 16 Measured rotor temperature at the upper measurement position during cycling while varying the hold time t_{15k} at 15,000 rpm with $I_B = 2.4$ A.

Since the upper measurement position is between the axial and the upper radial AMB, whereas the lower measurement position is below all major loss-inducing components, the temperature rise at the upper position is bigger than at the lower position (cf. References 4,5). The rotor reaches 94°C at the upper position after 387 cycles in less than 3 h with $I_B = 3.5$ A. Reaching the same temperature with $I_B = 2.4$ A takes 806 cycles and more than twice as long. This illustrates the strong impact of I_B on the rotor temperature. Reducing I_B also reduces the temperatures of the AMB stators, which are shown in Figure A4. This helps to reduce the rotor temperature since the stator also emits thermal radiation to the rotor, which increases with the stator temperature.

The rotor will reach a steady state temperature above 100°C even with $I_B = 2.4$ A. To safely prevent overheating of the permanent magnets of the PMSM, the temperature should remain well below 100°C. To further reduce the temperature, the test cycles can be adjusted by increasing t_{15k}, since the losses at 15,000 rpm are smaller than at 30,000 rpm.[4] This temperature reduction can be seen in Figure 16, in which the upper rotor temperature is shown during long-term cycling with $I_B = 2.4$ A. The shown measurement is a direct continuation of the one from Figure 15 with the same I_B. After the rotor reached 94.7°C, t_{30k} was reduced to 1 s and t_{15k} increased to 21 s, which led to a decrease in the rotor temperature. Then t_{15k} was incrementally reduced until the rotor temperature started to rise again. $t_{15k} = 12$ s led to a steady state temperature of approximately 91.5°C and $t_{15k} = 11$ s to approximately 92.5°C. Hence, if the steady state rotor temperature below 92°C is targeted, a full cycle takes 33 s, which includes the acceleration and deceleration time of 10 s each as well as $t_{15k} = 12$ s and $t_{30k} = 1$ s. With $I_B = 2.6$ A, $t_{15k} = 17$ s is required to stay below 92°C. Hence, by reducing I_B from 2.6 to 2.4 A, the time for a full cycle is reduced from 38 to 33 s, which reduces the total time it takes to test 200,000 cycles (see Section 1) by 11 days.

5 | DISCUSSION

The goal of the described procedure was to reduce the rotor temperature of a magnetically levitated spindle for fatigue tests during long-term operation. The focus was on reducing the bias current I_B of the radial AMBs. To assure a stable operation with different I_B, the controller must also be adjusted. This was done using a parameter optimization of a predefined controller structure. The presented optimization process considers the limitations and the speed-dependent dynamics of the system as well as its sensitivity function. The optimized controllers show a smaller maximum gain of the sensitivity function and are less susceptible to noise compared to a previously experimentally adjusted controller. For the described system, the smallest I_B for which a permissible controller was found is 2.4 A. Note that high I_B (here $I_B > 4.4$ A) also obstruct a robust control of the AMBs. Measurements show that the increase in rotor temperature during cycling can significantly be reduced by decreasing I_B. This in turn allows to considerably shorten the time it takes to perform 200,000 test cycles by reducing the hold time at 15,000 rpm. The focus of this article was on an AMB system, but the described controller design process can also be applied to other systems which are subject to strong parameter variations and for

which a simple controller structure is desired (e.g., References 26,29). However, the controller design process has some drawbacks and limitations:

- The optimization process can take significantly more time than a normal $\mathcal{H}_\infty$-optimization (for the described system 2 days instead of a few minutes). This is partly due to the iterative process for the parameter optimization, but also due to the high order and dimension of the combined system. However, it has to be considered that a $\mathcal{H}_\infty$-controller with comparable tolerance to parameter variations would be much more conservative. For the described system no $\mathcal{H}_\infty$-controller with $\gamma < 1$ could be found that works in the entire speed range. A less conservative controller might be achieved via μ-synthesis (e.g., References 20,22), but the controller would again have a high order, the iterative synthesis process might take a long time and in rare cases might not converge (cf. References 24,35).
- In the described approach the requirement $\gamma \approx \Gamma(\Omega)$ is only checked at 300 discrete, equally distributed Ω_i in Ω_{ges}. Hence, peaks in $\boldsymbol{G}_{zw}$ or S_{ii} might be missed if they only affect a speed range which is smaller than 1000 rpm. For the investigated system, the evaluation was repeated at 971 discrete, equally distributed Ω_i in Ω_{ges} for the optimized controllers with I_B equal to 2.1, 2.4, 3.0, 4.3, 4.4 A as well as 6.5 A and no such peak could be found. However, this might not be true for other systems.
- The optimization cannot distinguish between local and global minima, hence, there might be permissible controllers for smaller I_B than 2.4 A for the investigated system.

Only one fixed controller structure and equal I_B for the upper and lower AMB were considered in this article. Different controller structures or allowing dissimilar I_B for the upper and lower AMB might enable further reductions of I_B. Further reductions might also be achievable by reducing the amplitudes of the disturbance inputs, for example, reducing the influence of unbalance by utilizing an unbalance compensation method[43] or reducing measurement errors by compensating the sensor runout.[44] The safety factors which were introduced for the control current and the voltage are partly necessary to ensure that the system remains stable when the system parameters change due to high rotor and stator temperatures. These safety factors might be reduced when further models for the high-temperature behavior of the AMBs are considered in the optimization process. This can also be done for other changes or nonlinearities in the system (cf. Reference 37).

ACKNOWLEDGMENTS

This research was funded by the German Federal Ministry for Economic Affairs and Energy, grant numbers 03ET6064A and 03EI3000A. Open Access funding enabled and organized by Projekt DEAL.

CONFLICT OF INTEREST

The authors declare no potential conflict of interest.

DATA AVAILABILITY STATEMENT

Data available on request from the authors.

ORCID

Daniel Franz https://orcid.org/0000-0001-9534-847X

REFERENCES

1. Quurck L, Richter M, Schneider M, Franz D, Rinderknecht S. Design and practical realization of an innovative flywheel concept for industrial applications. Tech Mech. 2017;37(2–5):151-160.
2. Schneider M, Rinderknecht S. System loss measurement of a novel outer rotor flywheel energy storage system. Proceedings of the IEEE International Electric Machines & Drives Conference (IEMDC); 2019:1379-1385; IEEE.
3. Arnold SM, Saleeb AF, Al-Zoubi NR. Deformation and life analysis of composite flywheel disk systems. Compos Part B Eng. 2002;33(6):433-459.
4. Franz D, Schneider M, Richter M, Rinderknecht S. Thermal behavior of a magnetically levitated spindle for fatigue testing of fiber reinforced plastic. Actuators. 2019;8(2):37.
5. Franz D. Magnetgelagerter Schleuderprüfstand zur Untersuchung der Betriebsfestigkeit von Faserverbund-Rotoren (magnetically levitated test rig for the investigation of the fatigue strength of fiber composite rotors). TU Darmstadt, Dissertation; 2021.
6. Hagg AC, Sankey GO. The containment of disk burst fragments by cylindrical shells. J Eng Power. 1974;96(2):114-123.
7. Pichot M, Kramer J, Hayes RJ, Thompson RC, Beno JH. The flywheel battery containment problem. Proceedings of the SAE International Congress & Exposition; 1997.

8. Maslen EH, Schweitzer G. Magnetic Bearings: Theory, Design, and Application to Rotating Machinery. Springer; 2009.
9. Wilson B, Tsiotras P, Ferri-Heck B. Experimental validation of control designs for low-loss active magnetic bearings. Proceedings of AIAA Guidance, Navigation and Control Conference and Exhibit; 2005:1-20.
10. Hung JY, Albritton NG, Xia F. Nonlinear control of a magnetic bearing system. Mechatronics. 2003;13(6):621-637.
11. Jastrzebski RP, Pöllänen R. Compensation of nonlinearities in active magnetic bearings with variable force bias for zero- and reduced-bias operation. Mechatronics. 2009;19(5):629-638.
12. Charara A, de Miras J, Caron B. Nonlinear control of a magnetic levitation system without premagnetization. IEEE Trans Contr Syst Technol. 1996;4(5):513-523.
13. de Queiroz MS, Dawson DM. Nonlinear control of active magnetic bearings: a backstepping approach. IEEE Trans Contr Syst Technol. 1996;4(5):545-552.
14. Johnson D, Brown GV, Inman DJ. Adaptive variable bias magnetic bearing control. Proceedings of the 1998 American Control Conference (ACC); vol. 4, 1998:2217-2223.
15. Motee N de Queiroz MS. Control of active magnetic bearings with a smart bias. Proceedings of the 41st IEEE Conference on Decision and Control; 2002:860-865; IEEE.
16. Sahinkaya MN, Hartavi AE. Variable bias current in magnetic bearings for energy optimization. IEEE Trans Magn. 2007;43(3):1052-1060.
17. Siva Srinivas R, Tiwari R, Kannababu C. Application of active magnetic bearings in flexible rotordynamic systems – a state-of-the-art review. Mech Syst Signal Process. 2018;106:537-572.
18. Steyn SJM, van Vuuren PA, van Schoor G. Multivariable H∞ or centre of gravity PD control for an active magnetic bearing flywheel system. SAIEE Afr Res J. 2011;102(3):76-88.
19. Hirata M, Ohno T, Nonam K. Robust control of a magnetic bearing system using constantly scaled H-inf contol. Proceedings of the 6th International Symposium on Magnetic Bearings: ISMB6; 1998:713-722.
20. Lösch F. Identification and automated controller design for active magnetic bearing systems. ETH Zurich, Dissertation; 2002.
21. Sawicki JT, Maslen EH, Bischof KR. Modeling and performance evaluation of machining spindle with active magnetic bearings. J Mech Sci Technol. 2007;21(6):847-850.
22. Lanzon A, Tsiotras P. A combined application of H_infinit loop shaping and mu-synthesis to control high-speed flywheels. IEEE Trans Contr Syst Technol. 2005;13(5):766-777.
23. Mushi SE, Lin Z, Allaire PE. Design, construction, and modeling of a flexible rotor active magnetic bearing test rig. IEEE/ASME Trans Mechatron. 2012;17(6):1170-1182.
24. Maslen EH, Sawicki JT. Mu-synthesis for magnetic bearings: why use such a complicated tool? Proceedings of the ASME 2007 International Mechanical Engineering Congress and Exposition; 2007:1103-1112; ASME.
25. Nonami K, Ito T. μ synthesis of flexible rotor-magnetic bearing systems. IEEE Trans Contr Syst Technol. 1996;4(5):503-512.
26. Gahinet P, Apkarian P. Decentralized and fixed-structure H∞ control in MATLAB. Proceedings of the IEEE Conference on Decision and Control and European Control Conference; 2011:8205-8210; IEEE.
27. Duan G-R, Howe D. Robust magnetic bearing control via eigenstructure assignment dynamical compensation. IEEE Trans Contr Syst Technol. 2003;11(2):204-215.
28. Larsonneur R. Design and control of active magnetic bearing systems for high speed rotation. ETH Zurich, Dissertation; 1990.
29. Apkarian P, Gahinet P, Buhr C. Multi-model, multi-objective tuning of fixed-structure controllers. Proceedings of the European Control Conference (ECC); 2014:856-861; IEEE.
30. Genta G. Dynamics of Rotating Systems. Springer; 2005.
31. Chiba A, Fukao T, Ichikawa O, Oshima M, Takemoto M, Dorrell DG, eds. Magnetic Bearings and Bearingless Drives. Elsevier; 2005: 45-84. doi:10.1016/B978-0-7506-5727-3.X5000-7
32. Müller G, Vogt K, Ponick B. Berechnung Elektrischer Maschinen (Calculation of Electric Machines). 6th ed. Wiley-VCH; 2011.
33. Binder A. Elektrische Maschinen und Antriebe (Electric machines and drives). Springer; 2012.
34. ISO 14839-3:2006 Mechanical vibration—Vibration of rotating machinery equipped with active magnetic bearings—Part 3: Evaluation of stability margin; 2006.
35. Zhou K, Doyle JC. Essentials of Robust Control. Prentice Hall; 1998.
36. Sivrioglu S, Nonami K, Saigo M. Low power consumption nonlinear control with H∞ compensator for a zero-bias flywheel AMB system. J Vib Control. 2004;10(8):1151-1166.
37. Apkarian P, Noll D. Optimization-based control design techniques and tools. In: Baillieul J, Samad T, eds. Encyclopedia of Systems and Control. Springer; 2013:1-12.
38. Balas G, Chiang R, Packard A, Safonov M. Robust Control Toolbox 3: Getting Started Guide. The MathWorks, Inc.; 2011.
39. Apkarian P, Noll D. Nonsmooth H ∞ synthesis. IEEE Trans Automat Contr. 2006;51(1):71-86.
40. Barbaraci G, Pesch AH, Sawicki JT. Experimental investigations of minimum power consumption optimal control for variable speed AMB rotor. Proceedings of the ASME International Mechanical Engineering Congress and Exposition; 2010:1047-1056; ASME.
41. Freudenberg J, Looze D. Right half plane poles and zeros and design tradeoffs in feedback systems. IEEE Trans Automat Contr. 1985;30(6):555-565.
42. Jr Wall JE, Doyle JC, Harvey CA. Tradeoffs in the design of multivarable feedback systems; 1981. doi:10.2172/7061962
43. Herzog R, Buhler P, Gahler C, Larsonneur R. Unbalance compensation using generalized notch filters in the multivariable feedback of magnetic bearings. IEEE Trans Contr Syst Technol. 1996;4(5):580-586.

44. Setiawan JD, Mukherjee R, Maslen EH. Adaptive compensation of sensor runout for magnetic bearings with uncertain parameters: theory and experiments. J Dyn Syst Meas Control. 2001;123(2):211-218.

How to cite this article: Franz D, Jungblut J, Rinderknecht S. Controller parameterization and bias current reduction of active magnetic bearings for a flexible and gyroscopic spindle. *Advanced Control for Applications: Engineering and Industrial Systems*. 2022;4(3):e113. doi: 10.1002/adc2.113

APPENDIX A

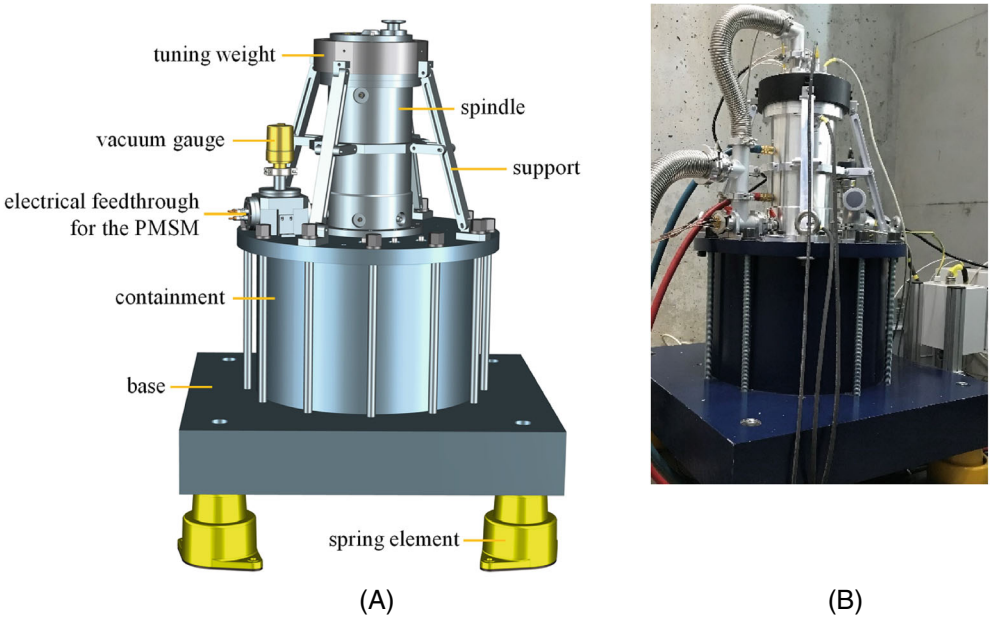

FIGURE A1 Outside view of the test rig: (A) model (rear view); (B) photo (front view)

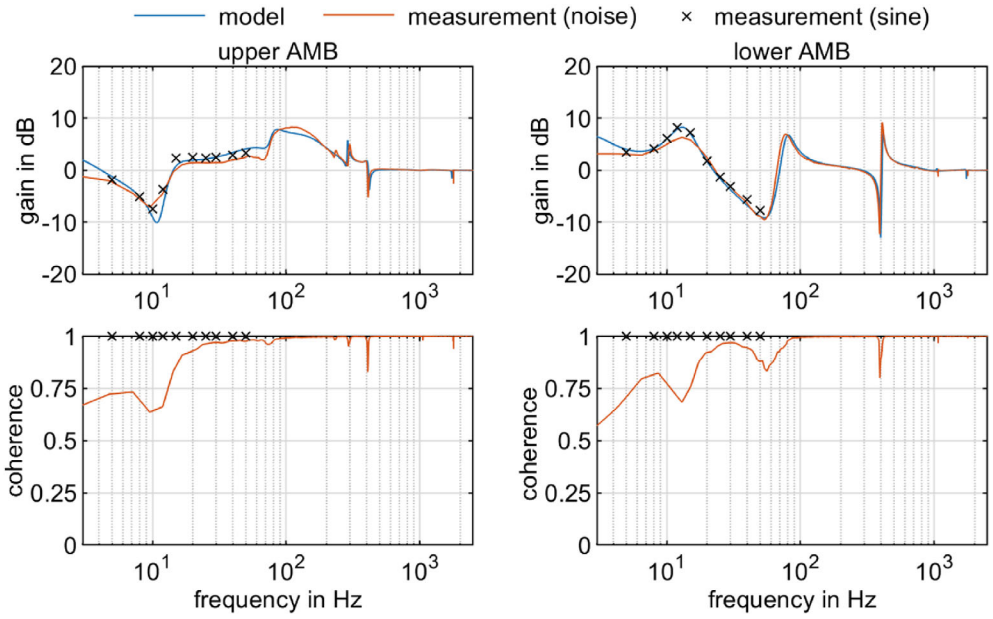

FIGURE A2 Simulated and measured diagonal elements of the sensitivity function of the AMBs at 0 rpm with $I_B = 4.3$ A and the respective optimized controller. The measurements were performed using noise and sinusoidal excitations

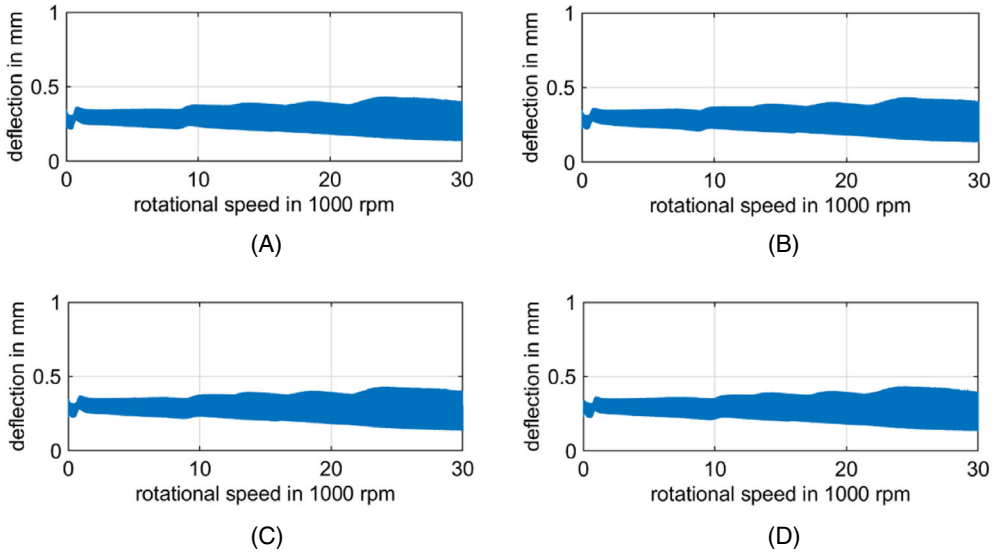

FIGURE A3 Measured deflection of the specimen during an acceleration from 0 to 30,000 rpm in 300 s with (A) $I_B = 2.4$ A, (B) $I_B = 2.6$ A, (C) $I_B = 3.0$ A, and (D) $I_B = 4.0$ A and the respective optimized controller

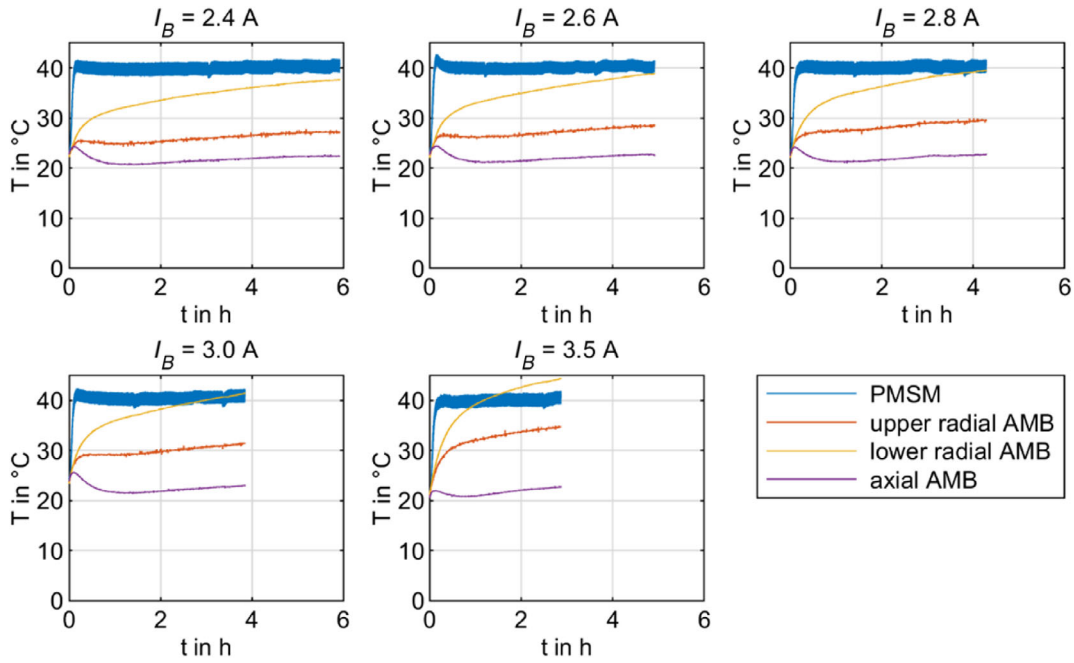

FIGURE A4 Measured stator temperature during cycling with different bias currents. The temperatures were measured with Pt100-sensores which are attached to the coils of the components

APPENDIX B

CHANGE OF THE OPTIMIZED CONTROLLER PARAMETERS WITH THE BIAS CURRENT

The parameterization of the optimized controllers varies considerably between some successive I_B, but certain trends are noticeable. The proportional and integral gain in the position controllers $C_{q,uu}$ and $C_{q,ll}$ (Figure 10A) increase with I_B. The proportional gain in $C_{q,ul}$ is in a similar range to the previous two for low I_B but decreases with I_B. The proportional gain in $C_{q,lu}$ is smaller than the other three for small I_B but increases with I_B. Hence, the proportional gains in $C_{q,lu}$ and $C_{q,ul}$ approach each other for increasing I_B and are comparable for $I_B > 5$ A. The differential feedback in $C_{q,ul}$ is negative for all

I_B. This is the only negative parameter in the optimized controllers. The cut-off frequency ω_c of the LP in $C_{q,ul}$ is around its minimum value of 10 Hz for all I_B. ω_c of the differential feedback LP in $C_{q,uu}$ is also low (< 100 Hz) for small I_B and increases with I_B. If this ω_c is reduced too much, the fourth forward mode (see Figure 3B) can be destabilized at high Ω. For $I_B \leq 2.6$ A, the proportional gain in the current controllers $C_{I,uu}$ and $C_{I,ll}$ are in the same range and decrease with I_B. However, for $I_B > 2.6$ A, the proportional gain in $C_{I,ll}$ increases with I_B, whereas it decreases further in $C_{I,uu}$. ω_c of the LP in $C_{I,uu}$ is between 600 and 900 Hz, whereas ω_c in $C_{I,ll}$ is above 10 kHz for most I_B and the LP was turned off.